SANDIA REPORT
SAND2009-6012
Unlimited Release
September 2009

Transmissive Infrared Frequency Selective Surfaces and Infrared Antennas: Final Report for LDRD 105749

David W. Peters, Paul Davids, Alvaro A. Cruz-Cabrera, Lorena I. Basilio, Joel R. Wendt, Shanalyn A. Kemme, William A. Johnson, G. Ronald Hadley, Sally Samora, and Hung Loui

Prepared by
Sandia National Laboratories
Albuquerque, New Mexico 87185 and Livermore, California 94550

Sandia is a multiprogram laboratory operated by Sandia Corporation,
a Lockheed Martin Company, for the United States Department of Energy's
National Nuclear Security Administration under Contract DE-AC04-94AL85000.

Issued by Sandia National Laboratories, operated for the United States Department of Energy by Sandia Corporation.

Available to DOE and DOE contractors from
U.S. Department of Energy
Office of Scientific and Technical Information
P.O. Box 62
Oak Ridge, TN 37831

Telephone: (865) 576-8401
Facsimile: (865) 576-5728
E-Mail: reports@adonis.osti.gov
Online ordering: http://www.osti.gov/bridge

Available to the public from
U.S. Department of Commerce
National Technical Information Service
5285 Port Royal Rd.
Springfield, VA 22161

Telephone: (800) 553-6847
Facsimile: (703) 605-6900
E-Mail: orders@ntis.fedworld.gov
Online order: http://www.ntis.gov/help/ordermethods.asp?loc=7-4-0#online

SAND2009-6012
Unlimited Release
Printed September 2009

Transmissive Infrared Frequency Selective Surfaces and Infrared Antennas: Final Report for LDRD 105749

David W. Peters, Paul Davids
Applied Photonic Microsystems

Alvaro A. Cruz-Cabrera, Joel R. Wendt, Shanalyn A. Kemme, Sally Samora
Photonic Microsystems Technologies

Lorena I. Basilio, William A. Johnson
Electromagnetic Effects

G. Ronald Hadley
RF/Optoelectronics

Hung Loui
SAR Sensor Technologies

Sandia National Laboratories
P.O. Box 5800
Albuquerque, New Mexico 87185-MS1082

Abstract

Plasmonic structures open up new opportunities in photonic devices, sometimes offering an alternate method to perform a function and sometimes offering capabilities not possible with standard optics. In this LDRD we successfully demonstrated metal coatings on optical surfaces that do not adversely affect the transmission of those surfaces at the design frequency. This technology could be applied as an RF noise blocking layer across an optical aperture or as a method to apply an electric field to an active electro-optic device without affecting optical performance. We also demonstrated thin optical absorbers using similar patterned surfaces. These infrared optical antennas show promise as a method to improve performance in mercury cadmium telluride detectors. Furthermore, these structures could be coupled with other components to lead to direct rectification of infrared radiation. This possibility leads to a new method for infrared detection and energy harvesting of infrared radiation.

CONTENTS

FIGURES

NOMENCLATURE

ALD	atomic layer deposition
FDTD	finite difference time domain
FPA	focal plane array
FSS	frequency selective surface
HDP	high density plasma
HDR	hemispherical directional reflectance
HDT	hemispherical directional transmittance
HgCdTe	mercury cadmium telluride
MCT	mercury cadmium telluride
MIM	metal insulator metal
MoM	method of moments
PECVD	Plasma-enhanced chemical vapor deposition
PMMA	polymethyl methacrylate
PV	photovoltaic
RCWA	rigorous coupled wave analysis
RF	radio frequency
SEM	scanning electron micrograph

1. INTRODUCTION

Frequency selective surfaces (FSSs) are a common structure at microwave frequencies. We have taken these concepts and successfully adapted them for application in infrared systems. This work leveraged Sandia's prior work in infrared plasmonics. The resulting work shows the ability to add a metal layer to a surface and not increase the reflection at the design wavelength nor significantly affect the transmission. This occurs over a broad angular range from normal to near grazing. We refer to these designs as the transmissive FSSs. We also designed a series of FSSs that are highly absorptive at their design frequency. These structures hold promise in improving infrared detectors and perhaps infrared energy-harvesting rectifiers. The absorbing structures are antennas that perform at infrared frequencies, and we will refer to as infrared antennas. Both type structures involve surface plasmons, whose properties can be exploited for unique applications.

The transmissive FSSs offer a connected metal surface with a periodic array of apertures as shown in Figure 1. We could use such a surface to block electrical noise without affecting the performance of an optical device at the frequency that the FSS is designed for. This treatment of the surface is compatible with other surface treatments such as multilayer dielectric antireflection coatings so may be used in conjunction with them. This type FSS could also be used as the electrical contacts directly on top of an electro-optic device while not blocking the optical signal of interest.

Unlike many surface treatments, the single-layer FSS is remarkably angularly independent. When the angle of incidence (Figure 1) increases from normal to the surface towards grazing incidence we see little change in behavior. In traditional dielectric thin films there is a considerable shift that must be accommodated by making the structure increasingly complex. The different mechanism for transmission in the FSS explains this difference. Whereas a thin film stack relies on the interference of reflections between the many interfaces, the FSS relies on coupling from photons to plasmons to photons in the transmission of light from one side of the FSS to the other.

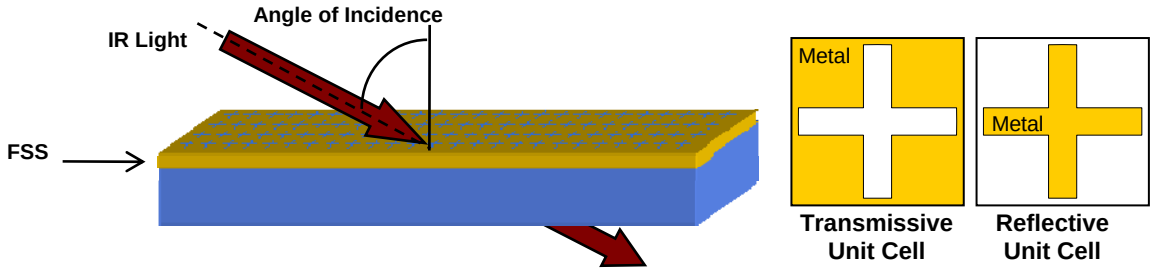

Figure 1. Basic schematic of a frequency selective surface on a substrate with incident light from any angle. At right are example unit cells for designs that are transmissive and reflective at their design frequencies.

In general FSSs may be multilayer devices with sheets of structured metal/dielectric with intervening layers of dielectric. Reflective FSSs tend to be comprised of metal structures in a

periodic array as shown in Figure 1. Transmissive structures, meanwhile, are the inverse, with a solid metal sheet with an array of metal apertures, also shown in Figure 1.

Infrared FSSs offer challenges not encountered in the microwave regime. Due to increased metal loss in this wavelength band there is a trade-off between the increased performance gained by having multiple layers with the loss associated with each metal layer. While a second layer may have increased our structures' performance somewhat, the added degree of complication for demonstration devices did not warrant the effort. Instead, we focused on optimizing single-layer metal structures. We then coupled our metal FSSs with dielectrics, thus proving the compatibility of the FSS with other antireflection technologies.

The simple addition of a ground plane and quarterwave lossy dielectric spacer transforms the transmissive FSS into an absorber at the design frequency and thus forms an infrared antenna. If this dielectric is a photoconductor, then the absorbed photons create carriers. The metal ground plane and patterned FSS layer form the contacts through which these carriers may be swept out. This geometry is a thin, spectrally-selective detector.

The further addition of a dissimilar metal plasmon waveguide under the FSS layer could lead to a rectifier working at infrared frequencies (30THz). When this rectifier is coupled with the infrared antenna we refer to the integrated device as a rectenna. A rectenna is capable of taking incoming radiation and producing a rectified signal and thus power. The rectenna could be a method for heat-into-power, or if biased could act as an infrared detector.

This report will describe the design, fabrication, and characterization of both transmissive FSS and infrared antenna structures. Results are compared to simulation. The transmissive designs are covered first, as the absorptive designs are extensions of the transmissive ones. In the final section before the summary we include some work from outside this LDRD to show where this work may be integrated with other concepts to form an infrared rectenna.

2. DESIGN METHODOLOGY

Initial designs were adapted from radio frequency (RF) designs in the literature. However, these designs do not have to deal with the loss associated with metals in the infrared. By being able to assume a lossless metal, RF designs are oftentimes many layers of alternating metal and dielectric. In the infrared, each additional metal layer adds a loss mechanism. Designs in the infrared must therefore be limited to a very few metal layers (one or two). We limited our efforts to a single patterned metal layer.

Modeling was primarily performed using two algorithms, method of moments (MoM) and rigorous coupled wave analysis (RCWA). The MoM code is EIGER™, a code written and maintained by Sandia and the University of Houston. The RCWA code is Matlab based; the source code was purchased from the code developer by Sandia for a previous project.

Other methods such as finite difference time domain (FDTD) are not well-suited to periodic problems such as these where off-normal simulations are required. However, FDTD was used to model the structures at normal incidence to determine where the electric fields are concentrated in the structure: of particular importance in the absorbing designs.

For instances when a three-dimensional visualization of the electric field was required, a discretized Helmholtz equation code was used. This Sandia-written code utilizes a unique iteration scheme to make large problems that can not currently be solved by direct matrix inversion possible. This code works for on-axis and off-axis illumination. For this project it was used to determine the behavior of phase fronts through the FSS elements. Flat phase fronts imply that the elements can be used in an imaging system. This was verified, as will be discussed later.

2.1 EIGER Simulations

We used EIGER™ for much of the early modeling efforts. EIGER™ is a parallel boundary-element code used at Sandia for a wide variety of electromagnetic problems. Results from this code were used for optimizing structure parameters. Three of the transmissive structures designed using EIGER™ are shown in Figure 2. These structures are periodic arrays, here we show the basic unit cell, which is then replicated in the two lateral dimensions. Dimensions for these structures were arrived at after some optimization using EIGER™.

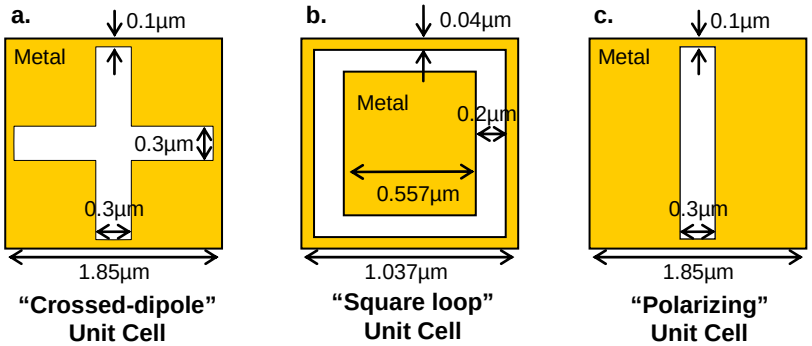

Figure 2. Unit cells for three infrared transmissive FSSs

The EIGER™ simulations helped us to understand important factors in the design such as the width of the aperture and other structure parameters. It also demonstrated the complexities of infrared FSS compared to their microwave counterparts. This is clearly shown in Figure 3, where the same structure is implemented using a perfect metal (a perfect electric conductor or PEC) and with actual refractive index values for gold in the mid-infrared. The resonance wavelength not only shifts, but the resonance widens, particularly on the long wavelength side. Simulations themselves become more difficult also as in the EIGER code fine meshes had to be used to correctly model the fields at the metal surfaces. For this reason, we could not simply blindly scale microwave designs to the infrared, although they offered a starting reference point.

This complexity was addressed in steps in our EIGER™ simulations. First, simulations assumed a planar PEC surface without a physical thickness. Then, a physical thickness was added to the PEC to match the thickness of the gold used in the physical devices. Finally, the PEC was changed to the lossy and dispersive real metal, in this case gold. At each step shifts in the response are seen.

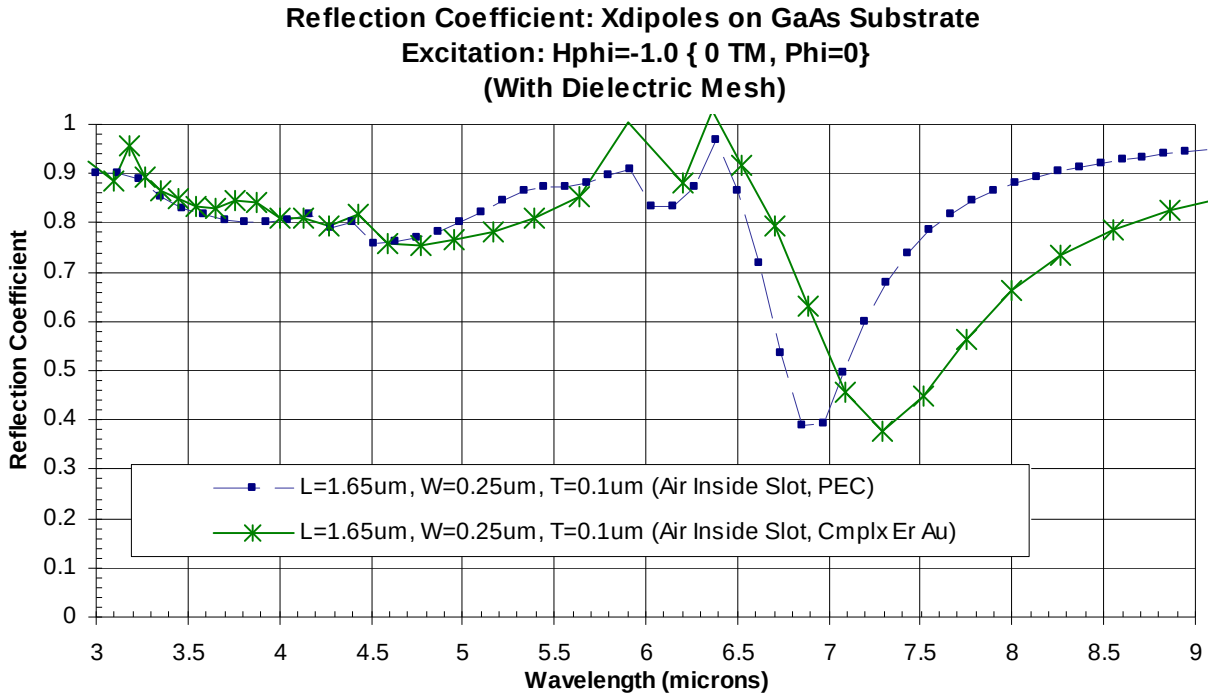

Figure 3. EIGER simulation of the reflection coefficient of the crossed-dipole FSS. The simulation compares a perfect electric conductor (PEC) for the metal layer to using measured values for gold. Note effect that the finite conductivity of the gold has on the resonance.

2.1.1 EIGER Code Development

Modeling of these structures required using the EIGER™ code to determine the reflection and transmission through the periodic structure. However, the code had not been used to calculate transmission through a structure where the bottom infinite half-space was not air. We therefore

had to modify EIGER™ to remove the assumption that the half-space below the FSS layer was free-space.

For the FSS problem EIGER™ divides the field up into an incident field (the direct field incident upon the FSS layer plus the reflected and transmitted fields due to the layered media) and a scattered field (the field scattered by surface currents on the FSS). In general, these surface currents are due to dielectric blocks or metallic structures comprising the FSS layer, which EIGER™ solves for by means of integral equations on the surfaces of the FSS structure. The incident plane wave impinging on the FSS from the upper half-space is denoted as the direct portion of the incident field, while the indirect portion of the incident field is associated with the remainder of the incident field.

The calculation of the indirect portion of the incident field is computed from transmission-line theory in the direction perpendicular to the layer using the direct portion of the incident wave as the source. For simplicity the direct incident wave is taken to be at the source location Z_{top}, where Z_{top} is the boundary between the upper half-space and the upper layer. Transmission-line theory then yields the solution for the fields at the observation point Z_{obs} for an observation point anywhere above or below the FSS structure. As is typical for these types of calculations, the transverse phase is not included in this transmission-line calculation.

The code was modified to calculate the total reflected and transmitted fields. For the (0,0) Floquet mode, this was done by adding the projection of the scattered field onto this Floquet mode to the indirect part of the incident field. For this calculation caution was taken to assure consistent phase conventions are used for both the scattered and incident fields. For higher-order propagating Floquet modes, the calculations of reflection and transmission required only the projection of the scattered field onto the corresponding Floquet mode.

2.2 RCWA Simulations

The majority of the simulations that were run for this project used rigorous coupled wave analysis (RCWA). RCWA is a common simulation technique for modeling periodic diffractive optics structures. This routine assumes an infinite periodic structure and linearity. For the FSS devices that we are investigating, these are valid assumptions as the device size is much larger than the period and no measurable nonlinear effects are present at our power levels. As the name implies this code is a rigorous code; where outside the aforementioned assumptions, the only approximation comes by limiting the number of modes (in effect limiting the terms in the expansion of the fields). The number of modes required for a particular problem is determined by running test cases with different numbers of modes. Mode number is increased until convergence is obtained. For these problems it was determined that 13 modes was sufficient. This number makes the problem size tractable with a high-end desktop workstation.

For all simulations both orthogonal polarizations are simulated. With the exception of the polarizing FSS the average of the two polarizations is plotted. This more closely aligns to real-world situations where light is generally unpolarized. For the polarizing FSS, both polarizations are shown.

The simulation of the crossed-dipole FSS at normal incidence is shown in Figure 4. The primary peak occurs around 8μm. Higher-order modes begin to propagate at shorter wavelengths as seen in the transmission peaks below 6μm. We made no attempt in the design process to tailor or suppress these higher-order modes.

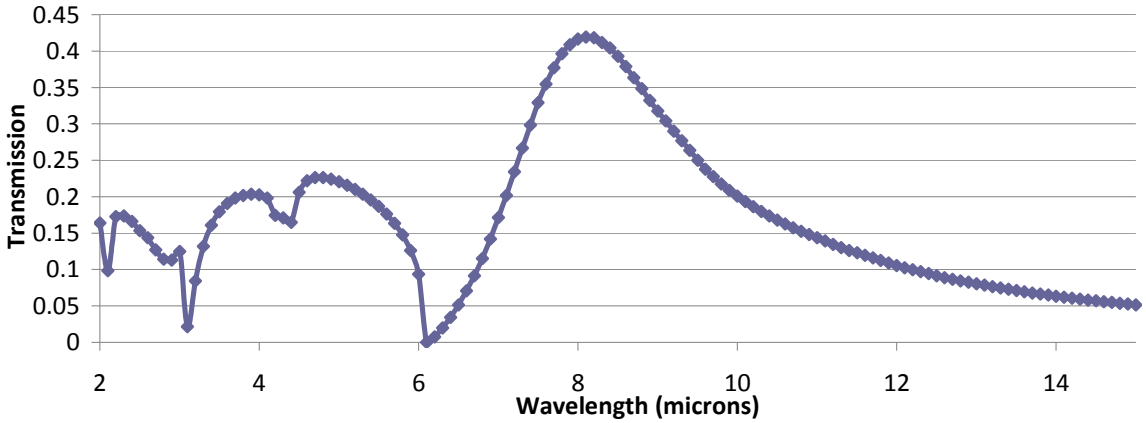

Figure 4. Transmission through crossed-dipole FSS with lateral dimensions as shown in Figure 2 and a gold thickness of 100nm on 1.5nm of oxide.

The polarizing FSS was designed to be a single-dipole version of the crossed-dipole. Note that the polarization whose electric field is perpendicular to the slots (perp. in Figure 5) is near identical to the transmission peak of the crossed-dipole FSS in Figure 4. However, the opposite polarization now has near-zero transmission. This would imply a polarizer with an extremely large extinction ratio. Scattering from non-ideal surfaces is not accounted for in this simulation, so we will revisit the extinction ratio in the measured data of this design where all non-idealities are present.

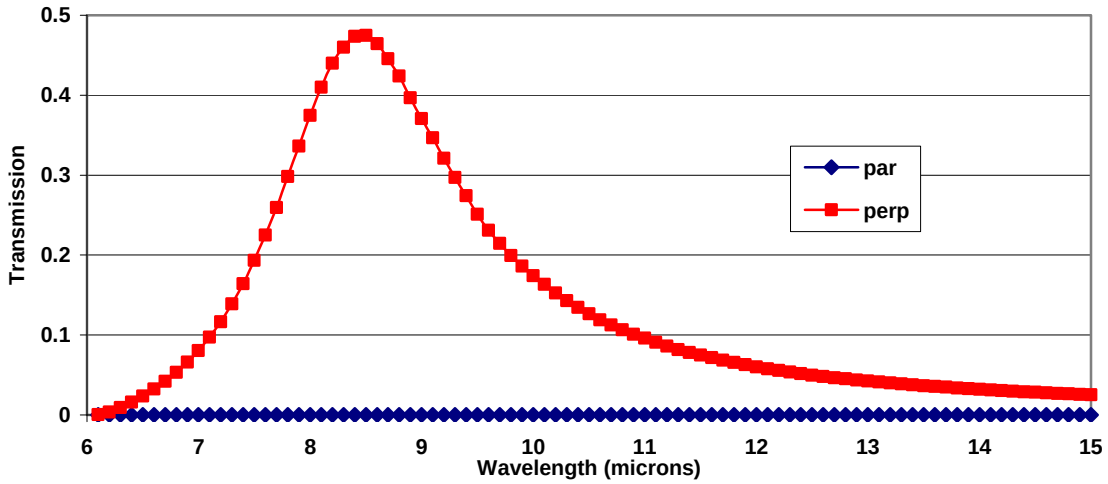

Figure 5. RCWA simulation of transmission for each polarization (with electric field parallel and perpendicular to slots) at normal incidence through the polarizing FSS design.

The final transmissive FSS, the square-loop design, leads to higher transmission over a larger bandwidth than the crossed-dipole design. The transmission for this design is shown in Figure 6.

The transmission at the design frequency is 64%. For bare GaAs this percentage is 71%. We have therefore created an electrically-thick metal layer on an optical surface that has a very small impact on the transmission of light through that surface. The 7% that is not transmitted is partially reflected (4%) and partially absorbed by the metal (3%).

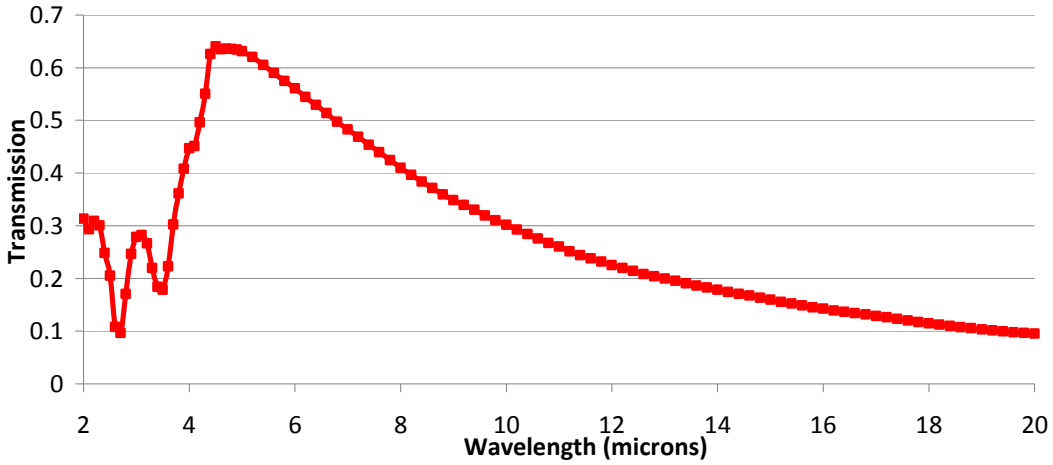

Figure 6. RCWA simulation of transmission of average polarized light through square-loop FSS.

2.3 Phase Front Simulations

In order for these FSSs to be used in an imaging system, not only must overall transmission be considered, but the phase fronts through the FSS must be investigated. If phase fronts become distorted then it would preclude the use of these devices in an imaging system, except for immediately before an FPA or other detector. We used an iterative Helmholtz equation code to demonstrate flat phase fronts through the FSS for normal and off-axis illumination.

The complex Jacobi iterative method[1] was recently introduced to provide iterative solutions of the Helmholtz Equation for three-dimensional problems where direct matrix inversion methods are prohibitive due to memory constraints. The previous derivation was appropriate for normal dielectrics, providing reasonable convergence rates for well-posed problems. However, the recent interest in metallic structures has led to the need to generalize this technique, since standard convergence parameter values result in divergent behavior.

We present here an updated derivation valid for metallic structures and use the resultant numerical method to analyze transmission of mid-IR light through a frequency-selective surface (FSS). Such structures offer a means of controlling the spectral transmission and polarization properties of a surface for mid-IR imaging using a single patterned metallic layer deposited on a dielectric substrate. While common in RF applications, their extension to the infrared is relatively recent and particularly challenging since the behavior of the (non-ideal) metal must be explicitly modeled. Frequency-domain modeling by solution of the 3D Helmholtz Equation represents a useful alternative to FDTD simulation for these structures. However, adequately resolving the skin depth of the metal results in a very large band matrix, whose solution requires an iterative method.

2.3.1 Numerical Method

The (non-preconditioned) complex Jacobi iterative method is described by the two-step formula[1]:

$$H^{n+2} = \left[1 - \frac{A}{4\alpha^*}\right]\left[1 + \frac{A}{4\alpha}\right] H^n \tag{1}$$

where *A* is the normalized Helmholtz operator

$$A \equiv \frac{\delta_x^2 + \delta_y^2 + \delta_z^2 + k^2}{\frac{1}{2}\left(\frac{1}{\Delta x^2} + \frac{1}{\Delta y^2} + \frac{1}{\Delta z^2}\right)}.$$

The δ's are the discretized finite difference second derivatives, and α is a complex convergence parameter. The stability of this scheme may be described in terms of the eigenvalues of A, written as $4(\psi + i\xi_i)$, where $\psi \equiv \xi_r - 2\sin^2\delta$, the subscripts r,i denote the real and imaginary parts, respectively, δ is a generalized spatial frequency, and

$$\xi \equiv \frac{k^2}{2\left(\frac{1}{\Delta x^2} + \frac{1}{\Delta y^2} + \frac{1}{\Delta z^2}\right)}.$$

It may be shown that optimum convergence results from maximizing $-\alpha_i / |\alpha|^2$ subject to the stability constraint $\alpha_i^2 < \alpha_r^2 - \frac{\psi^2}{2}$, where the value of ψ depends upon the spatial frequency in question and stability is required for all frequencies. For normal dielectrics the most restrictive condition occurs for the highest spatial frequencies, for which ψ = -2, resulting in the optimum $\alpha = (\sqrt{3}, -1)$. However, for metals ξ_r is no longer negligible due to the large negative dielectric constant in the metallic regions. For such problems the modified optimum convergence parameter is $\alpha = \left(\frac{\sqrt{3}}{2}, \frac{-1}{2}\right)\max|\psi|$ and the convergence rate is correspondingly slower. Problems involving the use of a preconditioner[1] also behave differently in the presence of metallic materials, and similar modifications to the preconditioning parameter are presently under study.

2.3.2 FSS Simulation

We have employed the complex Jacobi iterative method with modified convergence parameter as described above to examine the transmission properties of FSSs for mid-IR imaging. The particular structure being modeled is the one shown in Figure 2b.

The simulation was performed by solving the semivectorial Helmholtz Equation on a problem region consisting of a single unit cell in the lateral dimensions and 20μm in size in the depth dimension. Excitation consisted of a tilted plane wave at the incident (air) boundary directed parallel to one of the symmetry axes, and periodic boundary conditions at the opposite

boundaries to allow a proper simulation of the entire structure. Ramped absorbing regions were added both in the air adjacent to the incident boundary as well as in the semiconductor substrate. Simulation parameters were λ_o = 5μm, minimum grid sizes (in the metal) of 0.02μm, ε_{diel} = 10.75, ε_{metal} = -1161 + 212i on a 53 x 53 x 101 grid. Solutions were obtained to acceptable error tolerance within about 2 hours on a workstation without the use of parallel processing.

2.3.3 Simulation Results

The transmission computed for this structure was around 40% despite the fact that the non-metallic regions were substantially sub-wavelength in size. As in other similar experiments, this enhanced transmission results from strong plasmonic effects. The simulations for this problem also show that significant plasmonic re-radiation takes place from the back surfaces of the metal, leading to a wavelength- and polarization-dependent transmission. However, since this device is intended to be used for imaging, it is of particular importance to examine the phase of the light exiting the problem through the substrate. The concern is that the metallic patterning might result in significant phase distortion, rendering the structure unsuitable for imaging purposes. That this is not the case can be seen in Figure 7, where we show phase contours cut through the middle of the pixel for an incidence angle of 30°:

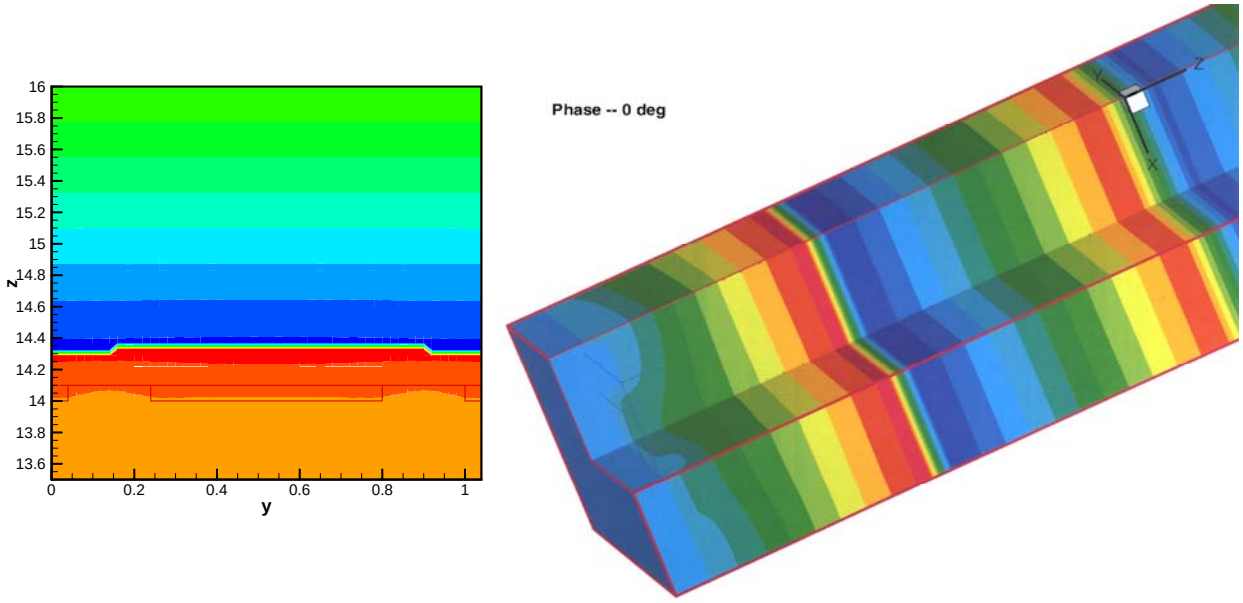

Figure 7. Phase fronts upon passage through the FSS of Figure 2b. Propagation is along the Z axis; units are in microns. Left image: FSS is seen in cross-section at 14μm; light is incident from the bottom. Right image: FSS is seen in cutaway at lower left. Note distortion of phase fronts in the immediate vicinity of the FSS due to evanescent fields, but otherwise flat phase fronts after transmission. Wavelength is 5μm.

The metal patterning is shown in black outline at a position of approximately 14μm. Although significant phase distortions do occur in the immediate vicinity of the metal layer, the exit phase fronts are uniformly tilted at an angle consistent with the dielectric constant of the substrate, implying that this FSS could serve well as an imaging device.

The complex Jacobi iterative method has thus been successfully employed to analyze a structure containing metals by a suitable modification of the convergence parameter. Although convergence is somewhat slower than for traditional dielectrics, one must keep in mind that solution of this problem by direct matrix inversion would require over 40 GB of memory and the inversion of a band matrix containing 2.6×10^9 elements. Such a large number of elements cannot even be enumerated using 4-byte integers.

3. FABRICATION

The transmissive designs were fabricated using liftoff to pattern the gold film. We targeted a gold layer of 0.1µm, ensuring the metal layer was optically thick across the waveband of interest. The liftoff medium was a 0.3µm layer of 495 polymethyl methacrylate (PMMA) that was spun at 4000 revolutions per minute (4% PMMA / 96% Chlorobenzene) on a 3 inch diameter double-side polished GaAs wafer.

The pattern was written into the PMMA using a JEOL JBX 9300FS e-beam writer operating at 100kV. The pattern used for liftoff is the reverse tone of the cross pattern shapes, accounting for 70% of the overall surface. The post-development cross patterns left behind serve as the liftoff layer. Writing this high a percentage of the pattern area is not attractive from either an exposure time or process latitude point of view. The dosage difference between barely removing the resist from the areas around the crosses and completely eroding the crosses is small, so it is difficult to control dimensions. However, a negative resist process where only the crosses themselves are written is not viable. It would be difficult to reliably achieve the 0.1 µm gaps between the cross arms due to resolution limitations of even an excellent negative resist such as NEB31. Furthermore, negative resist is not generally a good liftoff candidate due to its positively sloped sidewall and the fact that the resist has been crosslinked in the exposure and is not easily dissolved away.

After a post develop resist descum in ozone, a 0.1µm layer of gold was evaporated on top of the patterned PMMA. To better match the simulation code, we omitted the usual Ti adhesion layer and deposited the gold directly onto the GaAs. Liftoff was accomplished with acetone. The patterned gold FSS covered a relatively large 15mm by 15mm area. This area was necessitated by the need for testing the device at near-grazing angle incidence with a large enough beam to have sufficient power for detection.

The fabricated devices were imaged by SEM and the results are shown in Figure 8. The features of the cross shapes and the spacing between them were measured at different locations on the FSS and were averaged to determine the overall dimensions shown in Figure 3(b). A cleaved profile was used to estimate the thickness of the gold. Figure 9 shows the cleaved profile at 60 degrees and 90 degrees from the substrate normal. The two SEMs are at the same magnification and are aligned to help identify the features of the SEM in the part at 90 degrees. The image indicates a thickness of approximately 0.1 µm.

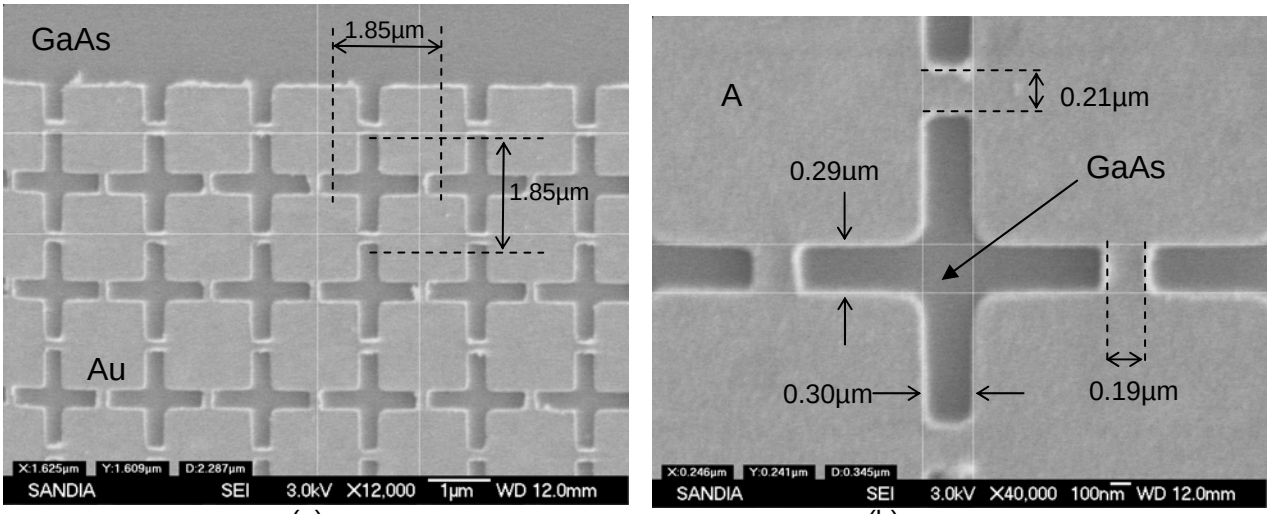

(a) (b)

Figure 8. SEM at the edge of the crossed-dipole FSS. (a) The periodic gold pattern on top of GaAs. (b) The average measured dimensions of the cross apertures and their spacing.

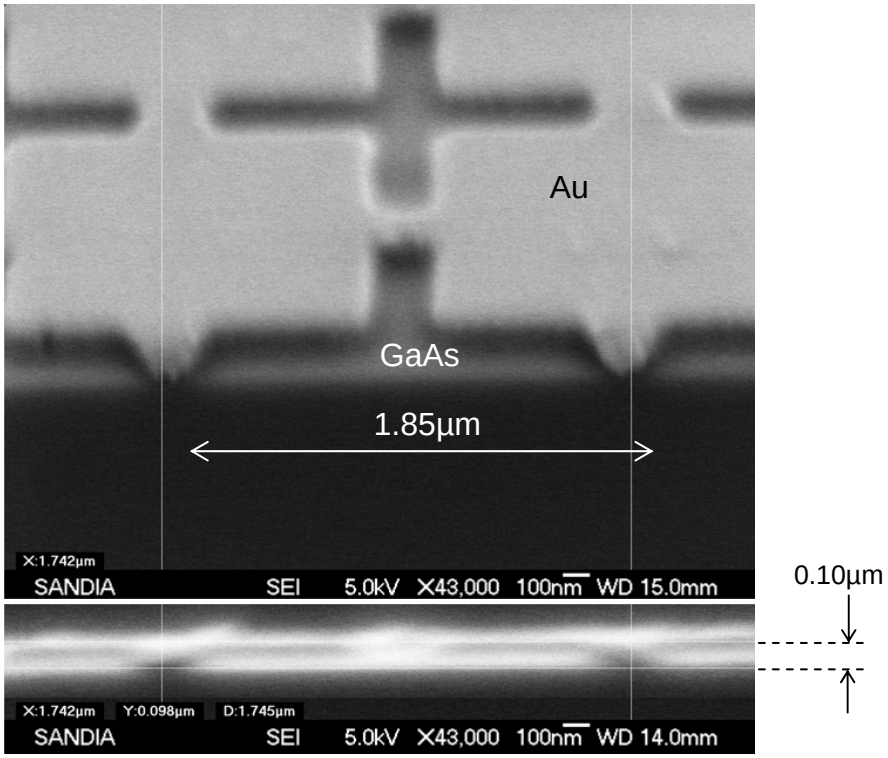

Figure 9. SEM image of crossed-dipole FSS at an angle of 60 degrees (top image), and 90 degrees (bottom image). The two images are aligned to indicate the nature of the structures in the image at 90 degrees. The measurement indicates that the gold layer is at least 0.1 µm thick, ensuring the metal is optically thick across the waveband of interest.

After struggling to optimize the PMMA process for the crossed-dipole FSS, we switched to an even higher contrast positive resist, ZEP520A, from Nippon Zeon, for the square-loop FSS design. The slightly wide process latitude using ZEP520A allowed better control of dimensions and more reliably higher yield liftoff. The thickness of the ZEP520A was 300 nm (5k rpm spin).

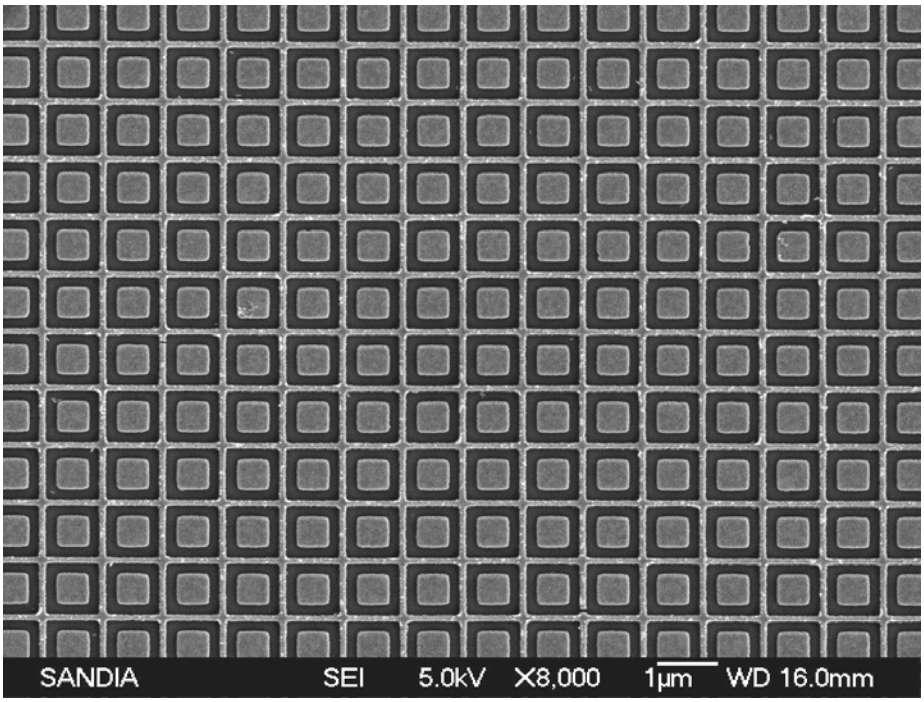

Figure 10. SEM of square-loop transmissive FSS design.

4. RESULTS FOR TRANSMISSIVE DESIGNS

In general, the results compare very well with the simulations. The agreement improved as time went on as better approximations of the structure and materials could be incorporated into the simulations. The single largest change resulted from the inclusion of the adhesion and oxide layers in the simulation. This topic is covered in detail in the following section.

All designs were tested with a SOC-100 using both the hemispherical directional reflectance (HDR) and the hemispherical directional transmittance (HDT) modes. The SOC-100 measures samples in a wavelength range of 2 to 25µm. The angular measurement capability of the HDR mode is limited to a range of 7° to 80° from normal. In HDT mode, the angular range is 0° to 70° from normal. To calculate absorption the angular range is 7° to 68°. To calculate absorption from the data we assume $A = 1\text{-}R\text{-}T$. This calculation may over predict actual absorption as some light may transmit or reflect at near grazing angles that are not measured in HDR or HDT modes.

4.1 Crossed-Dipole FSS

The crossed-dipole design of Figure 2a has a transmission maximum that is offset from that of the simulation. The difference can likely be attributed to oxide or adhesion layers not accounted for in this early simulation. Nevertheless the features of the measured and simulated curves track well as seen in Figure 11. Figure 12 shows the comparison of the reflectivity for the same device compared to the EIGER simulation. This simulation more closely predicts the peak of the resonance (seen as a dip since this is a plot of reflectance).

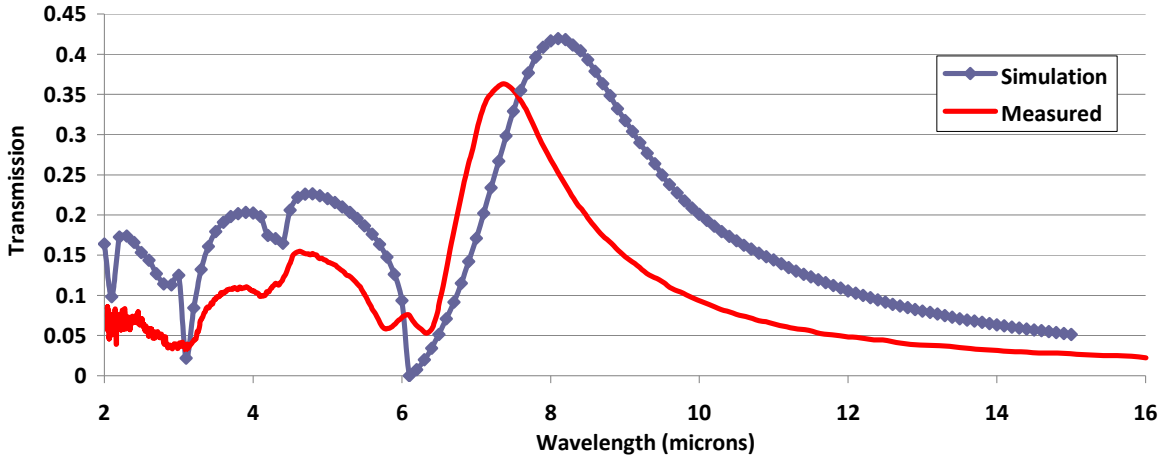

Figure 11. Measurement and simulation for crossed-dipole FSS at near-normal (8°) incidence.

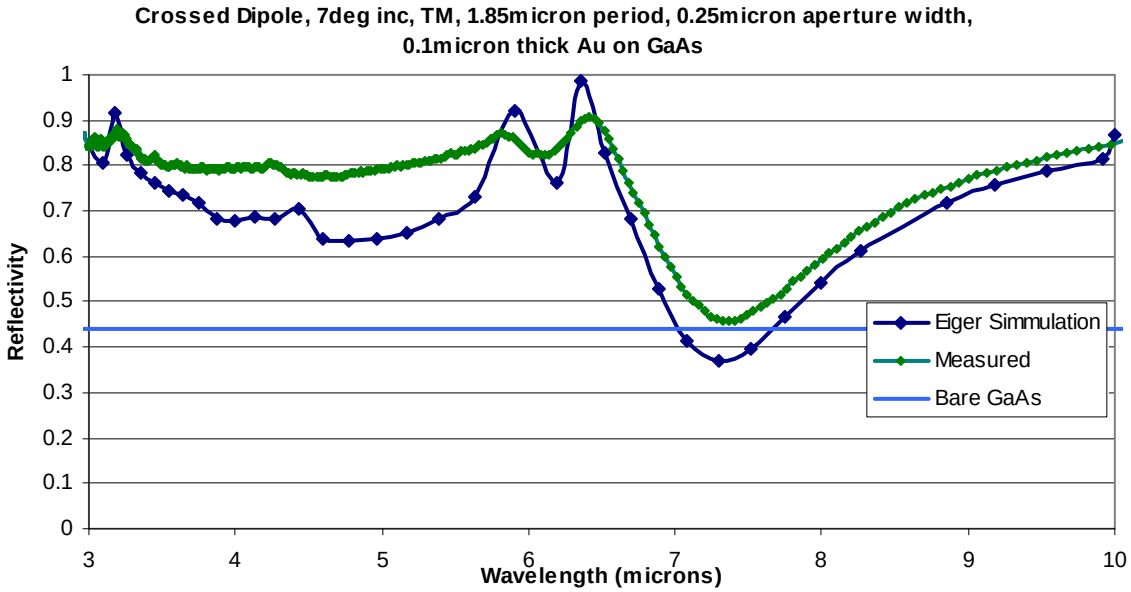

Figure 12. Measurement of reflectivity compared to EIGER simulation for crossed-dipole FSS.

The HDR and HDT measurements over a broad angular and wavelength range allow us to view much data in a compact form as seen in Figure 13. The horizontal axis is the wavelength, while the vertical axis is the angle of incidence. The reflectivity is denoted by the color. Here we see that even fine features at shorter wavelengths are seen in both the simulation and measured data. Black regions of the measured data plot are angles that the HDR cannot measure.

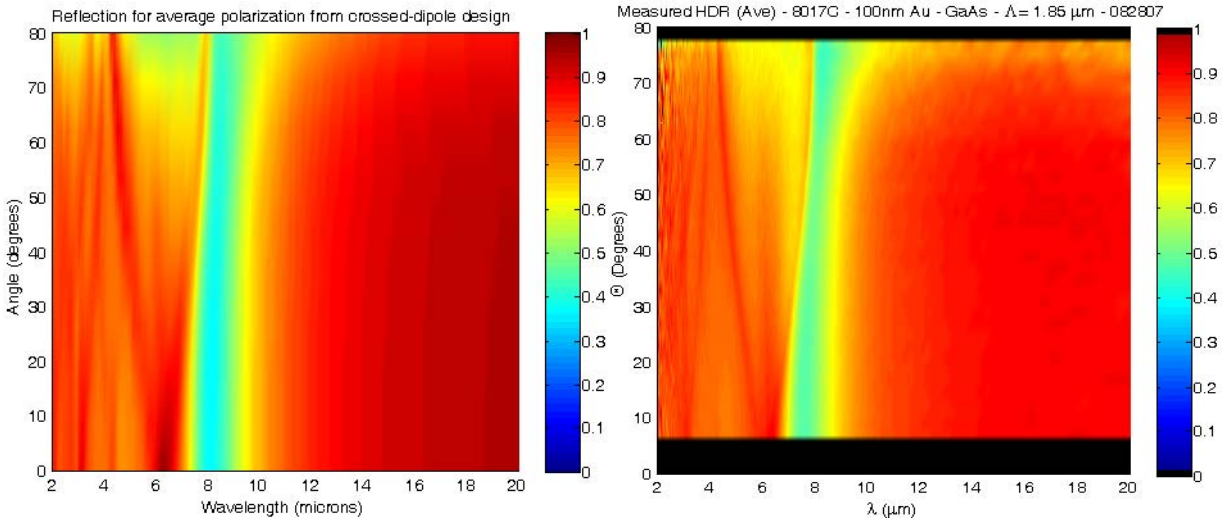

Figure 13. Plot of reflectivity as a function of wavelength and angle of incidence for the crossed-dipole FSS. At left is measurement, at right is RCWA simulation.

By adding a silicon nitride layer of quarterwave thickness to the top of the crossed-dipole FSS, we can demonstrate the independence of the FSS to other surface coatings such as dielectric thin films. In Figure 14 we see an increase in transmission after the SiN quarterwave is added to the sample. The transmission increases as it would if the dielectric coating were directly applied to

the GaAs without the intervening patterned gold FSS layer. In both cases the back surface of the double-sided polished GaAs wafer is untreated leading to a reflectivity of 28.5%.

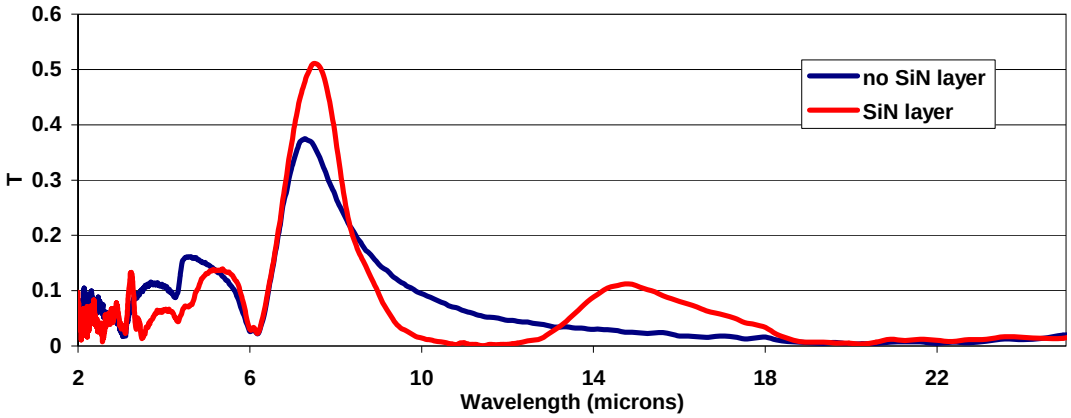

Figure 14. Measured transmission for the crossed-dipole FSS before and after a quarterwave layer of silicon nitride was applied. The backside of the GaAs is untreated in both cases (28.5% reflectivity).

4.2 Square-Loop FSS

To a greater degree than the crossed-dipole FSS, the square-loop FSS shows greater agreement between the simulation and measured results. Figure 15 contains both sets of data. At high angles the measurement begins to show a drop in transmission, however, as stated previously the HDT measurement is only valid to approximately 70°. Both simulations include the reflectance of the back face of the GaAs wafer. The transmission through the FSS is quite high over the entire angular range, with remarkably little deviation in the center wavelength.

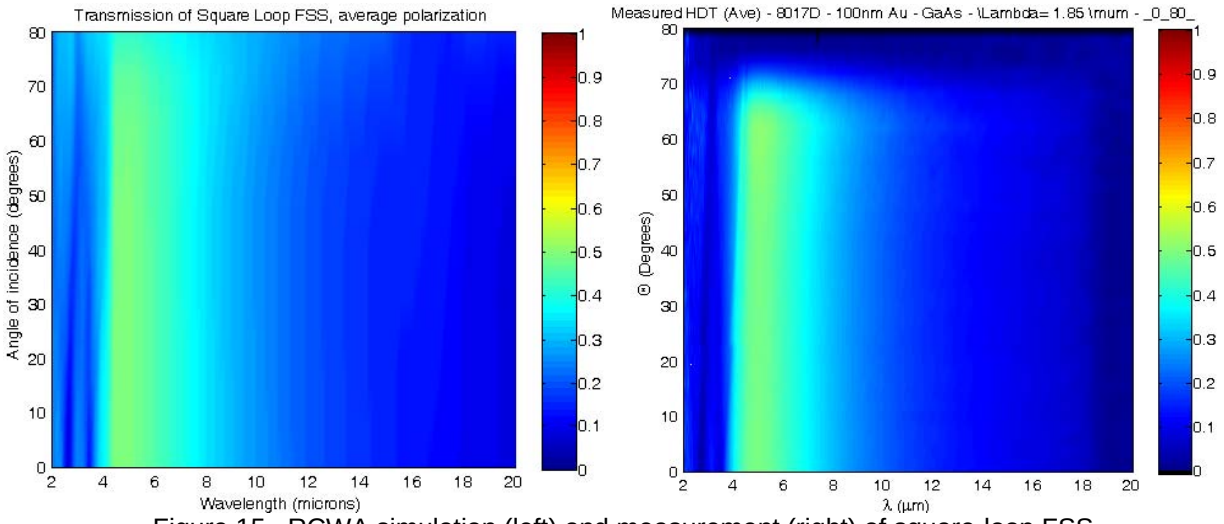

Figure 15. RCWA simulation (left) and measurement (right) of square-loop FSS.

A direct comparison of the simulation and measurement at normal incidence is in Figure 16. Note the closer agreement compared to the crossed-dipole simulation.

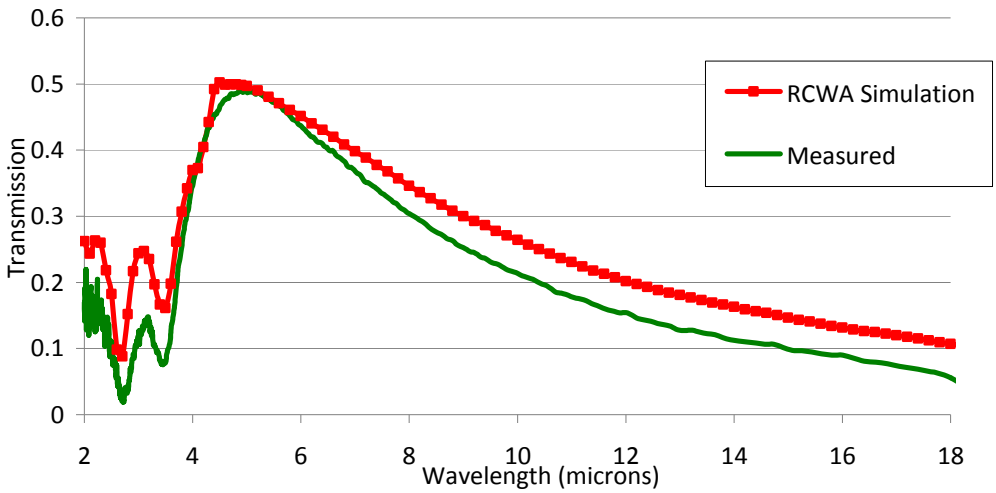

Figure 16. Simulation and measurement of reflectivity

4.3 Polarizing FSS

The polarizing design of Figure 2c led to a polarizer (seen in Figure 17) with wide angular acceptance at the design frequency as seen in the three transmission curves of Figure 18. These transmission curves include the reflection off of the untreated back surface. In Figure 19 we see the extinction ratio calculated by dividing the passed transmission by the blocked transmission. Due to the noise associated with measurement of the low power of the blocked transmission state, the extinction ratio plots also exhibit considerable noise. This is particularly true for the 60° case where one polarization is near the Brewster angle of the wafer and power levels are near zero.

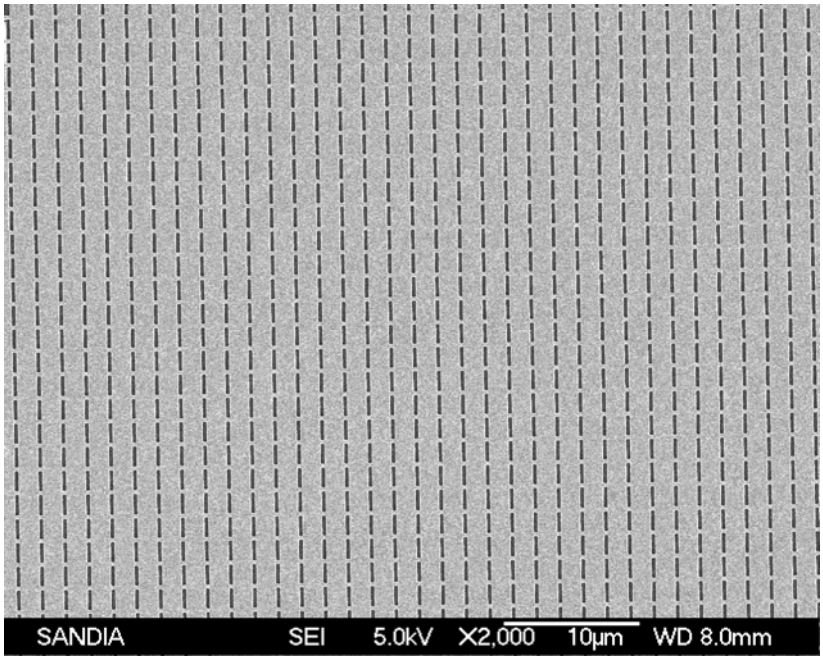

Figure 17. SEM of polarizing FSS.

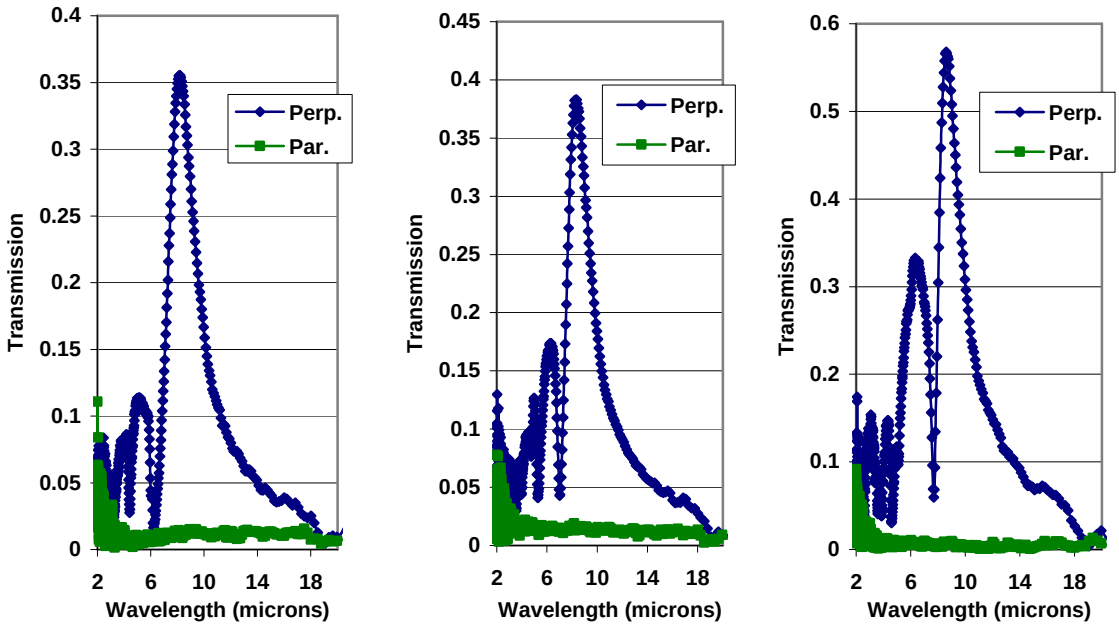

Figure 18. Measured transmission for the each polarization of the polarizing (dipole) design at normal incidence, 30°, and 60°. Transmission includes the back side of the wafer with its 28.5% reflectivity.

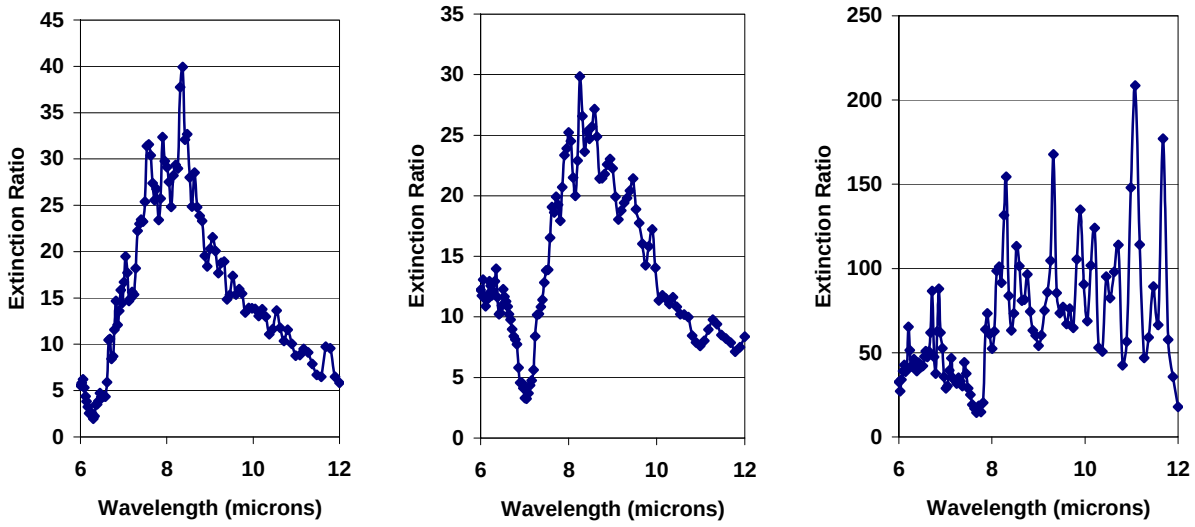

Figure 19. Extinction ratio for polarizing design at normal incidence, 30°, and 60°. Values are affected by noise in the low transmission of the TM case.

We have no reason to believe that this is an optimized polarizing FSS. The design is the polarizing version of the already studied crossed-dipole FSS and thus made for convenient comparison. For this purpose it performed well, exhibiting similar performance for the passed polarization state as did the crossed-dipole FSS. The design largely blocked the other polarization, however not entirely in practice.

4.4 Effect of Oxide and Adhesion Layers

Simulations were initially run with the gold directly on the GaAs and the crossed dipole structure was fabricated this way. However, a more reliable process includes a very thin (10nm) adhesion layer of titanium between the substrate and the gold layer. This layer is often ignored in simulations since it is so much smaller than the wavelength of light. In the case of FSS structures it is not possible to ignore this layer as surface modes have strong fields at the metal/substrate interface. By changing the nature of this interface through the addition of a metal with different properties the surface modes will be changed also, thus altering the resonant frequency of the structure. In addition to the titanium layer, there are oxide layers associated with the substrate and with the titanium adhesion layer. RCWA simulations were run where the thin titanium adhesion layer was included in the simulation. Further simulations were run that included the oxide layers.

One of the present oxide layers originates from native oxides that grow on the substrate. Silicon substrates have a well-known oxide layer that has been well characterized for the semiconductor industry. A similar oxide layer exists on GaAs, although thinner and less robust. We estimate a 1.5nm layer of this oxide is probably present on these wafers.

Additional oxides form as the titanium adhesion layer is deposited. Although deposited in a vacuum chamber, oxygen molecules are still present. These oxygen molecules combine with some of the titanium. A 10nm layer of titanium would therefore really be a sandwich of titanium oxide, titanium, and titanium oxide. The two titanium oxide (TiO_x) layers we estimate to be 1nm to 2nm thick. For the simulations we used a 1nm layer on either side of the Ti.

In the FSSs studied here, the effect of the adhesion layer is similar in magnitude to the shift seen in the metamaterial split ring resonator designs. For the simulation, we assumed a TiO_x thickness of 1.0nm above and below an 8nm titanium layer. The simulations shown in Figure 20 show a shift to shorter wavelengths when the sandwich of TiO_x and Ti are added to the simulation. The inclusion of the adhesion layer leads to simulations that more closely resemble the measured data. The simulation of gold directly on the GaAs substrate does not have good agreement with the resonant frequency of the measured data. The addition of the Ti layer shifts this resonance to be much closer to the measured resonance. The addition of the titanium oxide layers leads to changes in some of the curve features. As the 10nm of Ti and the Ti + TiO_x curves largely bound the measured curve, further refinement of the thickness of these layers could lead to an even closer agreement.

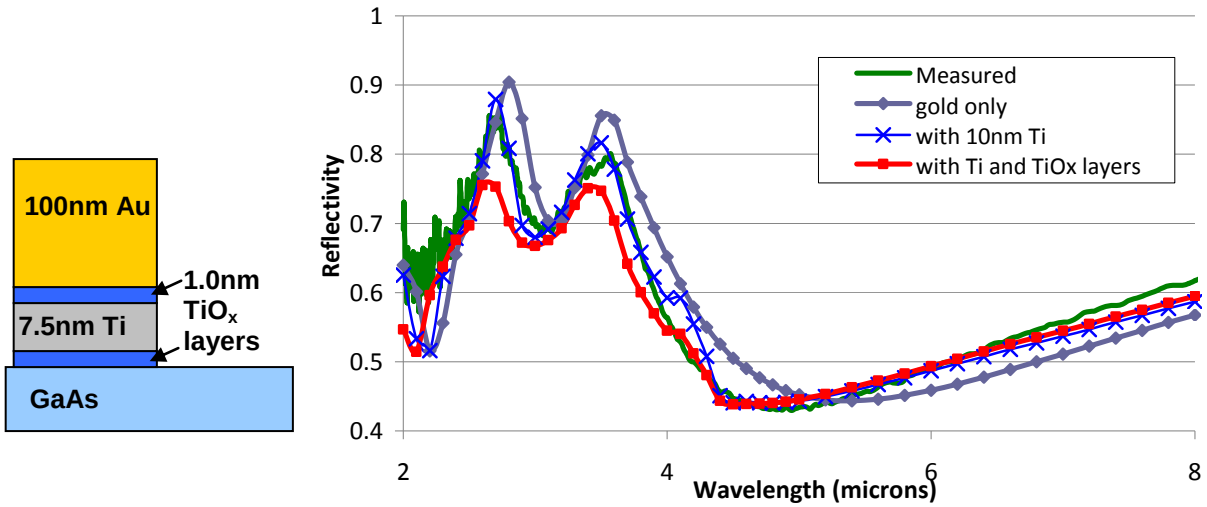

Figure 20. Schematic (not to scale) showing layers of Ti and TiO_x between the gold and GaAs substrate. At right, a comparison of simulations with and without TiO_x with the measured data. 1.25nm TiO_x layers are above and below a 7.5nm Ti layer. Reflectivity plots take into account a 28.5% reflectivity off of the back surface of the GaAs wafer.

5. INFRARED ANTENNAS FOR MCT DETECTORS

An infrared antenna offers several applications in sensor and infrared energy-harvesting applications. A large percentage of the incident energy in a certain wavelength band can be absorbed in a thin layer. For sensor applications this means that only a thin layer of active material such as HgCdTe is required. The smaller amount of material leads to a smaller dark current and a better performing device.

By using FDTD simulations we can see that the fields in these antenna structures are dominated by strong surface waves at the metal-dielectric interface. These surface waves may be channeled into thin surface plasmon waveguides. From here a travelling wave rectifier could transform the incident radiation to energy. While beyond the scope of this project, these applications demonstrate the utility of the FSS designs.

Through some simple adjustments to the highly transmissive designs we can achieve a spectrally selective absorber. This configuration could lead to highly efficient detectors and as a component in the direct rectification of infrared radiation, a potential energy harvesting method.

By adding a quarter layer of an absorbing material below the patterned metal layer of the prior designs and a metal ground plane as shown in Figure 21 we can transform the transmissive design into an absorptive one. The absorption occurs in the dielectric layer where the strong plasmonic fields lead to high absorption in a small volume. No transmission occurs since the bottom metal layer is thick enough to prevent any light penetration. Some optimization is required after this transformation, but this basic design, borrowed from RF Salisbury screen designs, is a starting point.

Figure 21. A representative unit cell for an infrared antenna. Absorbing dielectric thickness is roughly one-quarter of the freespace design wavelength divided by the index of the material. Dielectric can be a detector material such as HgCdTe.

Figure 22 shows the electric field strength simulated by FDTD. The electric field is strongest immediately under the apertures in the FSS layer. The surface plasmon modes bind this energy to the metal surface. The absorptive material between the two metal layers will strongly absorb this energy. Since it is bound to the surface rather than propagating, the amount of absorbing material required may be limited to these regions where the field strength is highest. This FDTD simulation was for one linear polarization, leading to the two high field areas on opposite sides of the central FSS square. The other linear polarization would have strong field strengths on the other two square sides. The symmetry of the FSS design allows us to take advantage of both polarization states.

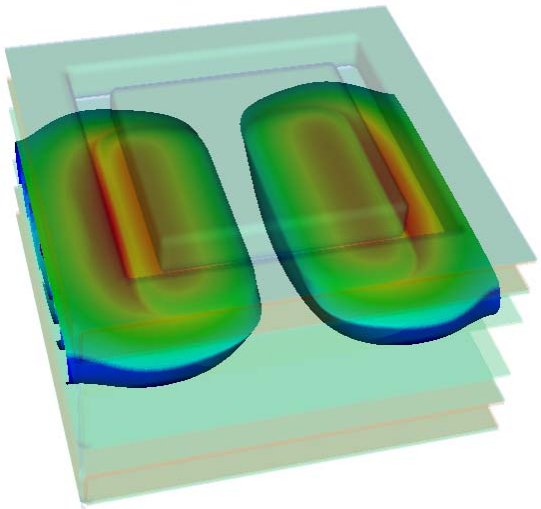

Figure 22. Electric field strength FDTD simulation of a square-loop absorbing design. Strong fields are seen at the bottom surface of the FSS layer.

5.1 Mercury Cadmium Telluride Detector Design

The connected geometry of the FSS top layer means that it can be used as one of the contacts on a detector and the solid metal back layer can be the other conductor. We modeled a detector structure using numbers for MCT supplied by a MCT grower. On either side of the active layer of MCT, a thin layer of inactive MCT is grown. This leaves an active layer of only 255nm as shown in Figure 23. The absorption as a function of wavelength is shown in Figure 24. Note the strong absorption (over 90%) at the design wavelength of 4.6μm. Also note that the absorption is polarization independent and angularly independent out to 25°, which is the coverage of an F/1 optic. The thin volume of active MCT used in this design means that the dark current will be less than that of a bulkier configuration. Furthermore, spectral bands could be changed pixel-to-pixel by changing the FSS geometry.

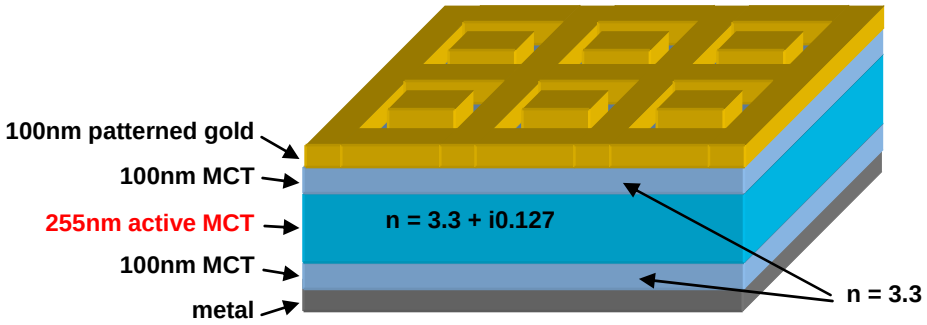

Figure 23. Mercury cadmium telluride detector design with an absorption peak at 4.6μm.

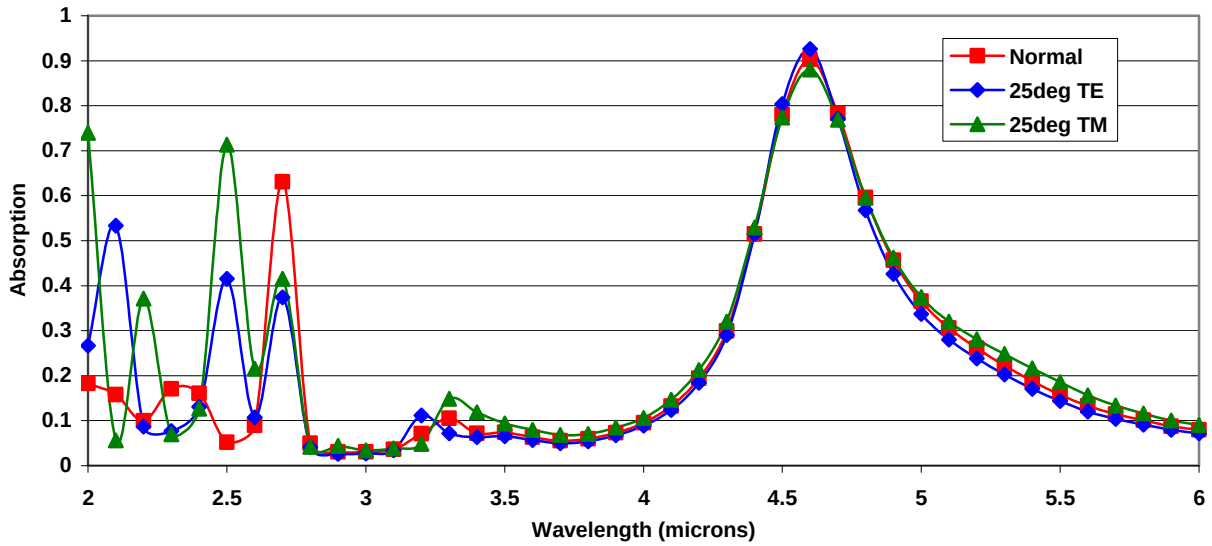

Figure 24. Absorption for the infrared antenna of Figure 23. Note strong absorption at the design wavelength of 4.6μm for angles across an F/1 optic's field of view.

5.2 Silicon Dioxide and Silicon Nitride Designs and Results

Our proof-of-principle infrared antenna designs are derived from the square-loop transmissive FSS of Figure 2b. We used silicon dioxide and silicon nitride for our absorptive layer. These materials were chosen due to their ease of deposition in our facility. Unfortunately, in the infrared their absorption profiles are quite complex with resonant features as seen in the peaks in the imaginary component of the refractive index of both materials in Figure 25. These features partially dictated the location and bandwidth of the absorption bands as the resonance associated with the FSS and the material resonances couple. A broadband infrared absorber such as HgCdTe would not have these issues.

Figure 26 shows the basic geometry for the HDP SiO_2 and PECVD SiN infrared antennas. thicknesses of the dielectric layer is dictated by the refractive index of the material at the design frequency. Generally a quarterwave thickness is desired. Figure 27 shows unit cells of the periodic pattern that were used for the SiO_2 and SiN designs. Different unit cells allowed us to verify more than one design experimentally and offered more points for comparison between simulation and measurement.

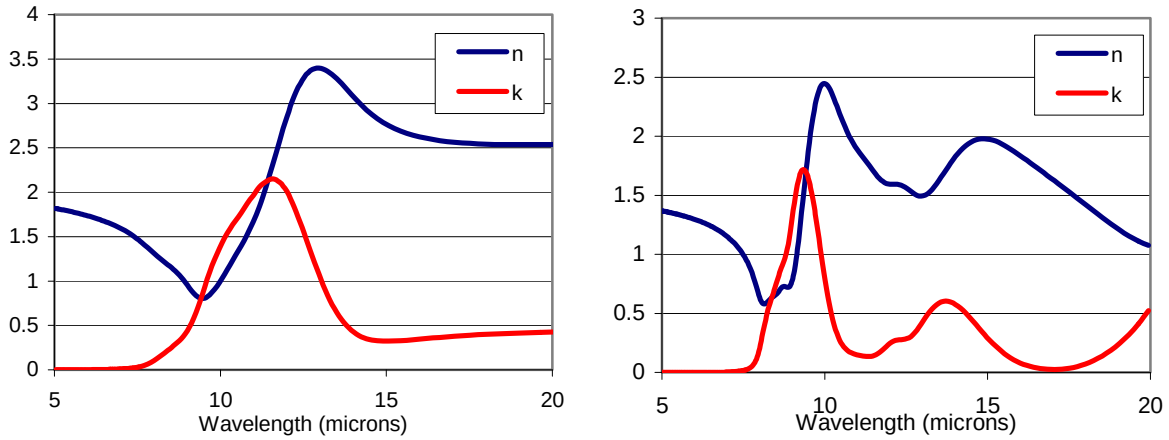

Figure 25. PECVD silicon nitride refractive index values (right) and HDP silicon dioxide refractive index values (left), where $n_{complex} = n + ik$. Measurements taken on Sandia deposited material.

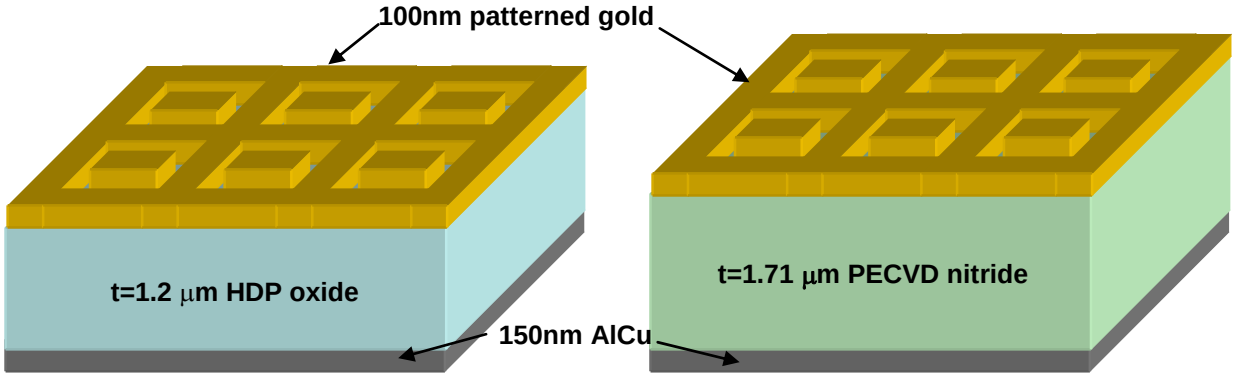

Figure 26. Side view schematic of silicon oxide and nitride infrared antenna designs.

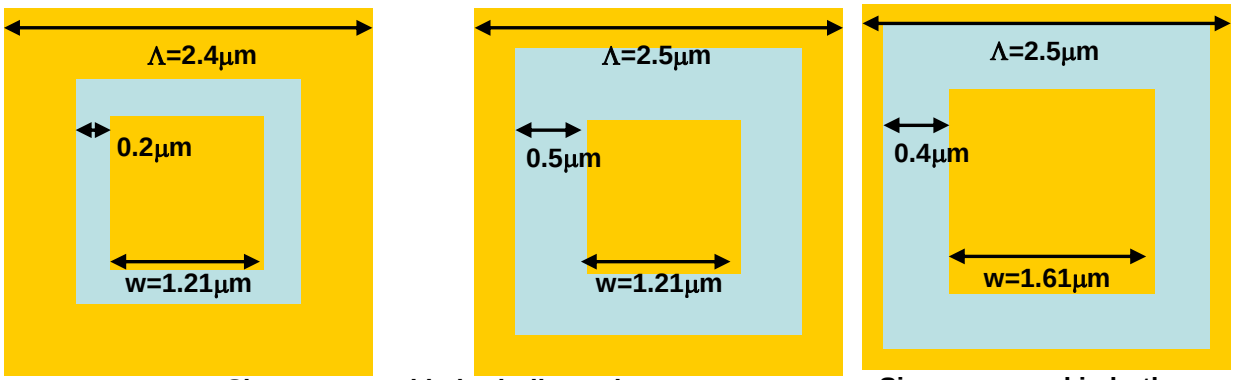

Figure 27. Dimensions of silicon oxide unit cells and silicon nitride unit cell.

These three designs were fabricated in their respective materials. The SEM of the SiN design after the exposure of the photoresist is shown in

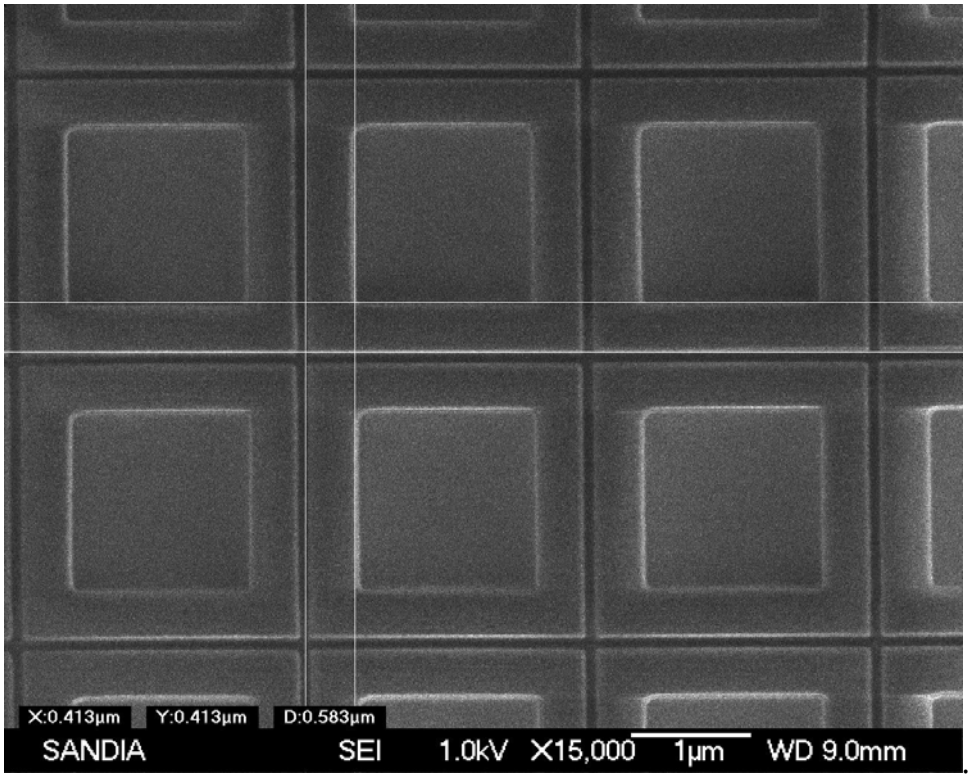

Figure 28. SEM of SiN infrared antenna design after the exposure of the photoresist.

Figure 29, Figure 31, and Figure 33 are the simulations that show the reflectivity of the three absorbing designs. Figure 30, Figure 32, and Figure 34 show the corresponding measured reflectivity for the three designs. Light that is not reflected is absorbed in these structures since there is no transmission. Therefore in all plots the areas of low reflectivity (blue) represent a region of high absorption. The measured data was obtained using the HDR as described at the beginning of Section 4. In the silicon nitride case we see a strong absorption at the design frequency of 8.4µm. This absorption is over 90%, yet only requires 1.71µm of SiN.

These multi-layered IR absorbing antennas, in Figures 29-34, are nearly completely independent of the angle of incidence and polarization. (Note, the near zero reflectance is for both s- and p-polarized averaged reflectance). This simple FSS based design results in a near perfect impedance match from free-space into the absorbing matched stack for arbitrarily incident light and cannot be achieved with complex multi-layered dielectric and metallic stacks. This large area antenna array structure can be used to couple into MCT diode sensor arrays and may be useful in direct conversion of IR radiation into DC current for thermal energy harvesting applications.

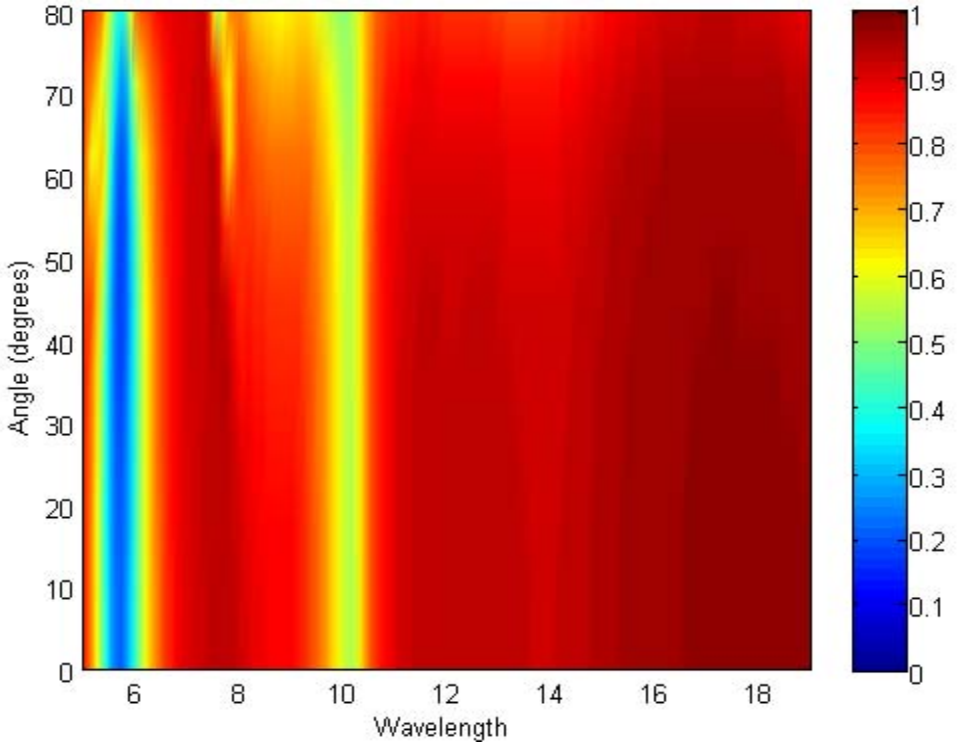

Figure 29. Reflectivity of light with equal TE and TM components from the SiO_2 Design 1 with omnidirectional absorption line at 10μm. Low reflectivity = high absorption.

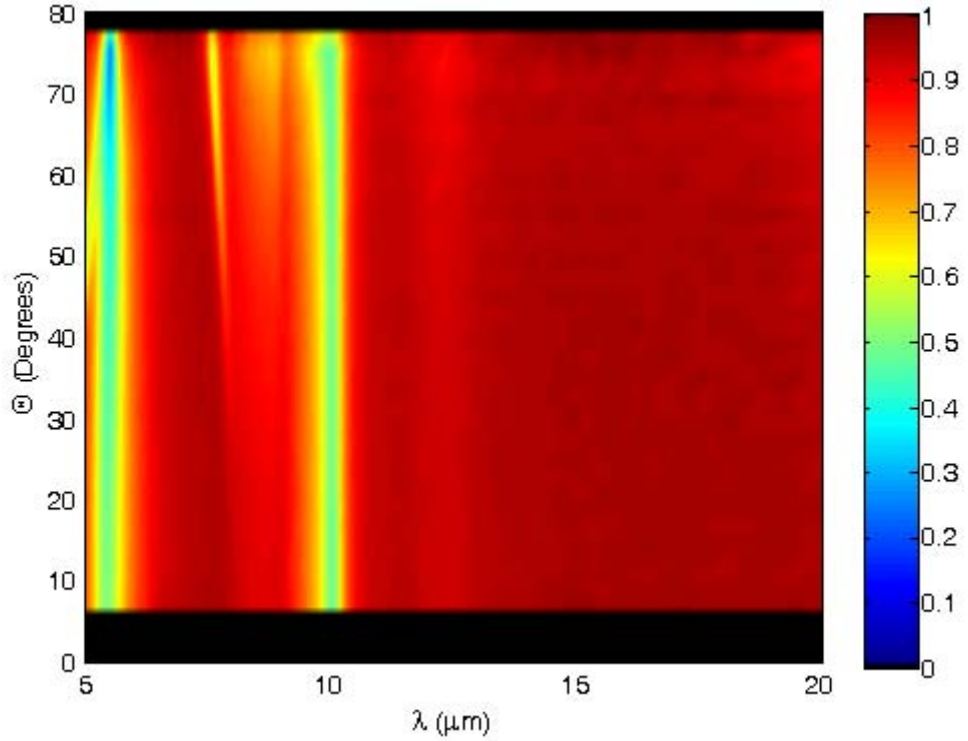

Figure 30. Measurement of the reflectivity using unpolarized light for the SiO_2 Design 1. Low reflectivity = high absorption.

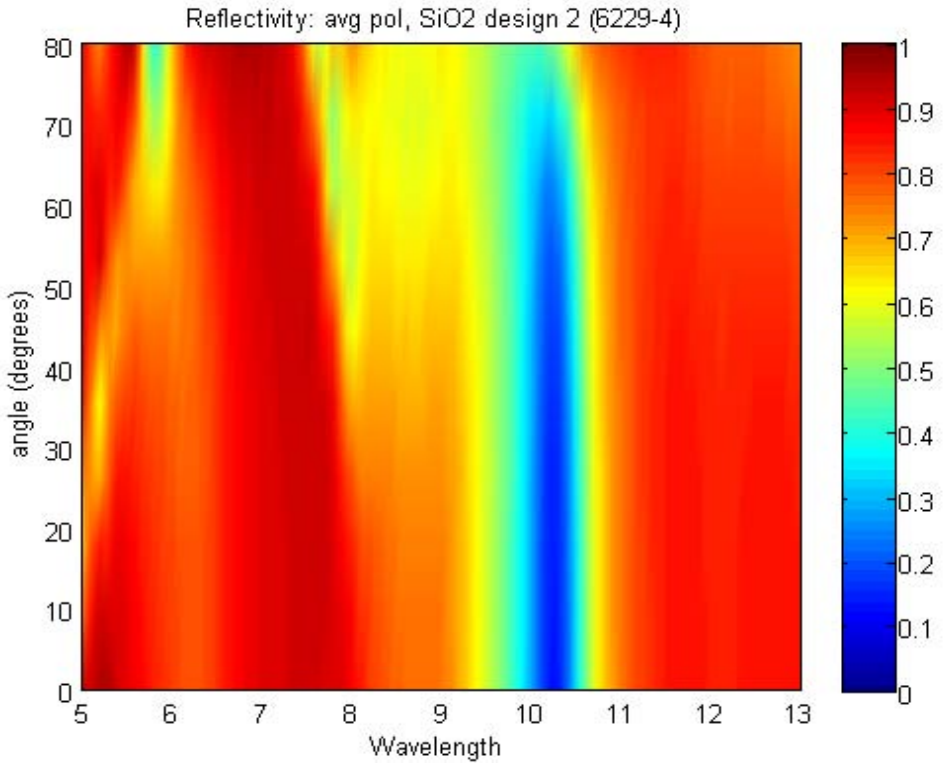

Figure 31. Reflectivity of light with equal TE and TM components from the SiO_2 Design 2. Note strong absorption line at 10.4μm. Low reflectivity = high absorption.

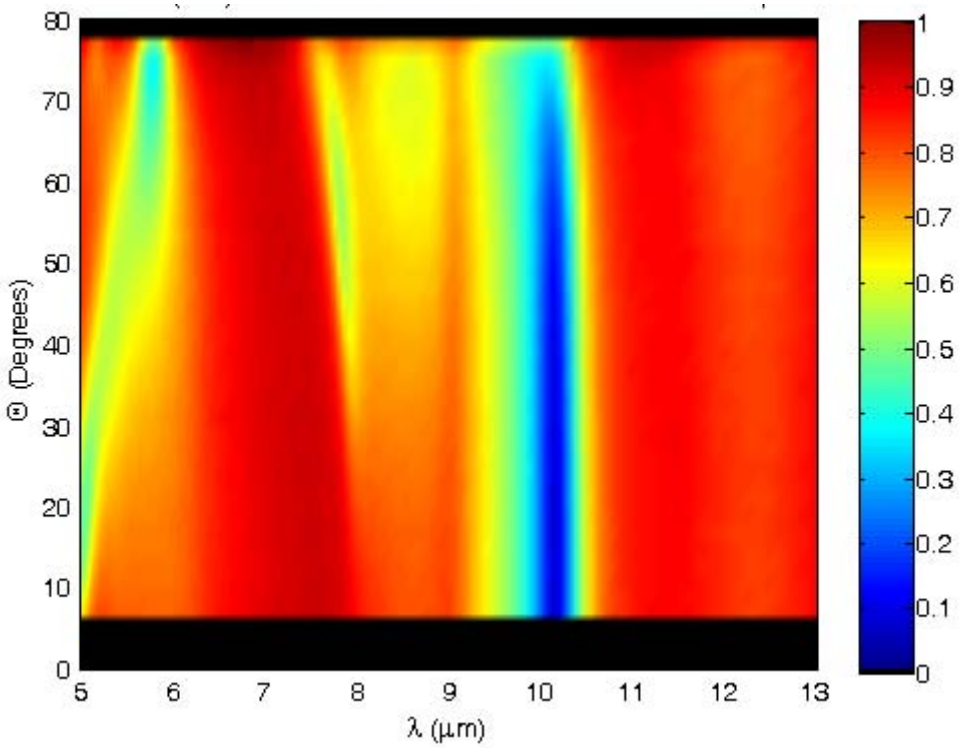

Figure 32. Measurement of the reflectivity using unpolarized light for the SiO_2 Design 2. Low reflectivity = high absorption.

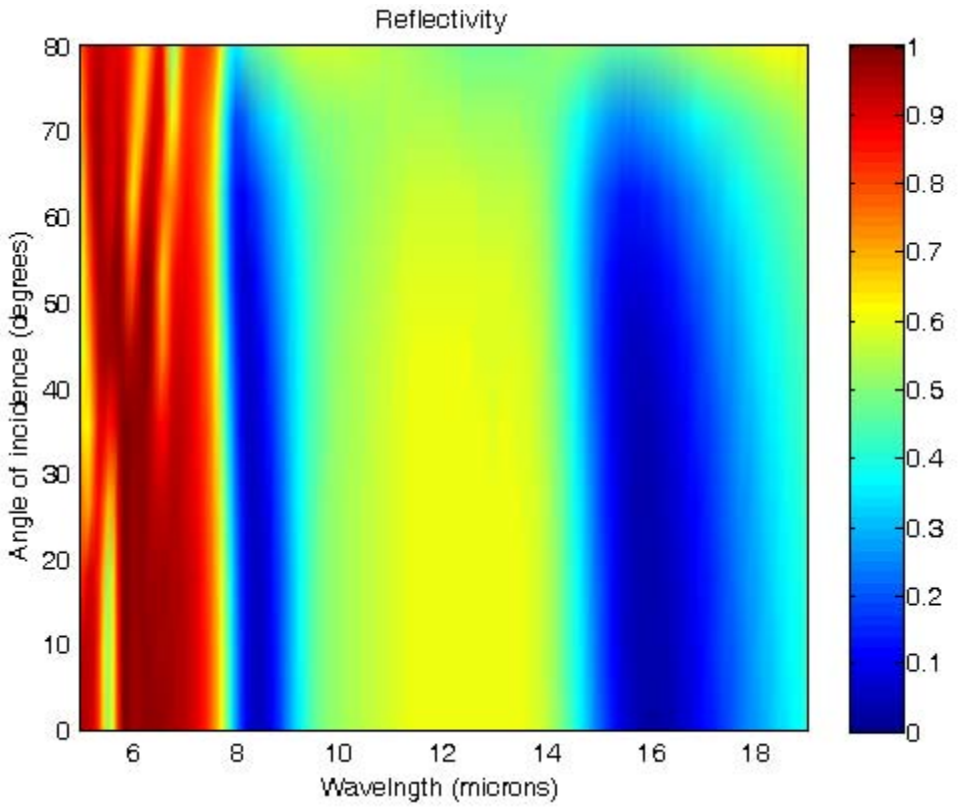

Figure 33. Reflectivity of light with equal TE and TM components from the SiN design. Absorption line was designed for 8.4μm.

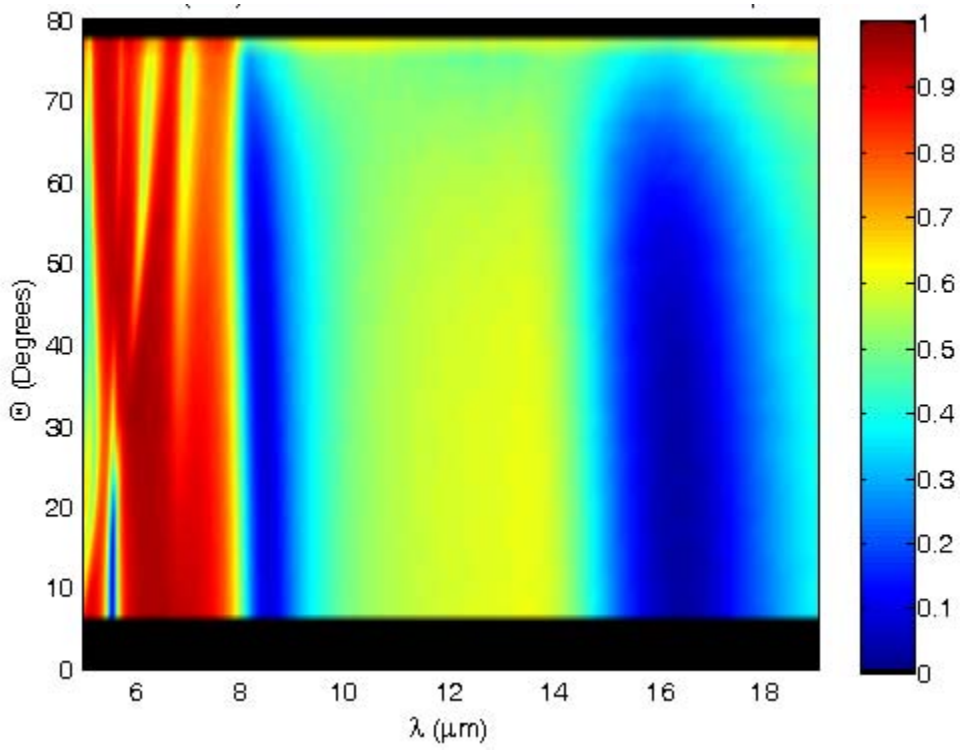

Figure 34. Measurement of the reflectivity using unpolarized light for the SiN design. Low reflectivity = high absorption.

6. DIRECT CONVERSION OF IR RADIATION FOR PHOTOVOLTAIC APPLICATIONS

Rectennas (rectifying antennas) are an area of research that offers large rewards if key roadblocks can be overcome. The infrared antennas that we have designed under this project could be an important component of a rectenna. We include with the IR antenna work done under this project, the work on the other components of the rectenna so as to present that entire picture. The other prime component addressed is the diode. This work was conducted outside this LDRD, but in conjunction with this work and will not be discussed in detail. Diode fabrication was performed at CINT under user proposal U2008A159: Surface Manipulation and Analysis of Atomic Layer Deposited Thin Films. Surface plasmon directional coupling simulations were performed by Paul Davids prior to his employment at Sandia.

The direct conversion of radiation into a useful DC current is a fundamentally different process than the usual photovoltaic absorption and carrier collection. Direct conversion represents a "coherent" detection scheme where the time varying electric field of the associated radiation is transformed into a voltage signal which is rectified by a non-linear element to give a non-zero DC current. This is in contrast to the typical "incoherent" photoabsorption process, where the incident radiation is absorbed, a process proportional to the intensity of the radiated electric field and which generates electron hole pairs which drift and diffuse in a built in electric field to generate the DC terminal current. Direct conversion of RF radiation through use of an antenna coupled to a rectifying element has been shown to be highly efficient, > 85% external efficiency at 2GHz. These devices are often called rectennas and consist of two main design elements, an antenna structure, and a rectifying diode. The antenna is designed to efficiently transfer incident power to the rectifying diode considered the load impedance. The diode must be fast enough to directly half wave rectify the voltage signal transmitted from the antenna. The question remains, is it possible to rectify with similar efficiency IR and visible light? In this report, we will examine our initial steps to answer this question and to construct new efficient IR energy harvesting and uncooled detector schemes.

A potential area of application of IR energy harvesting is to directly integrate the IR rectenna onto a multi-junction photovoltaic cell (PV). This is shown schematically in Figure 35. At right in Figure 35 there is a comparison of two blackbody spectrum at different temperatures. The spectrum for a cool body at 10 C has a peak emission at 10 microns, where as at 100 C the emission shifts to 8μm. Significant power exists in the mid-IR band from 3-5μm and 8-12μm. This waste energy if efficiently converted to DC current could lead to an efficiency improvement of the PV device. Typically, in a PV cell, thermal radiation from the incident solar spectrum, and absorption and re-emission in midwave IR pass through the PV cell. Converting this background IR radiation to useful energy would serve two purposes; Primarily, we obtain an additional DC current from the direct conversion of the thermal light improving the PV cell efficiency, and secondly, reduction in the operating temperature of the PV cell. This secondary thermal management improves the performance of the device by improving the temperature dependent mobilities of the electrons and holes. This thermal management is expected to impact the performance of the PV cell under concentration, when the cell can significantly heat up. Furthermore, the metallic nature of the IR rectenna readily allows for integration with the multi-junction PV cell and can be used to form the back-side contact to the cell.

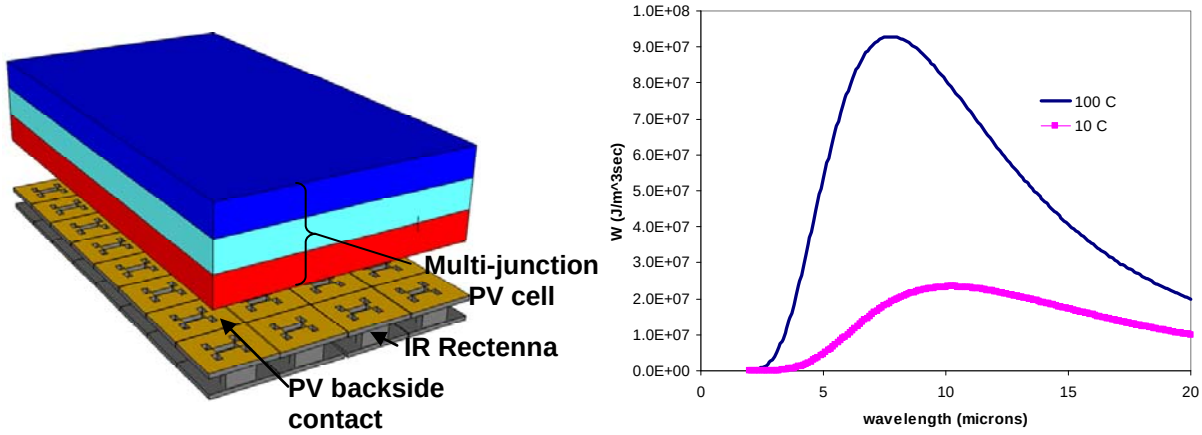

Figure 35. Schematic of a multi-junction PV cell with an integrated IR rectenna for thermal energy harvesting and temperature management. The metallic IR rectenna acts also as the backside contact to the PV cell. The inset shows the spectral exitance of a blackbody at 10 and 100 degrees C. Power in 8-12μm band is 327 W/m^2 and 92 W/m^2 for 100 C and 10 C respectively.

6.1 Problems Scaling RF Rectenna Designs to IR and Visible Wavelengths

Current attempts at scaling microwave rectenna designs to the IR and visible portion of the spectrum have not been successful. Direct conversion efficiencies of less than 1% have been reported. Figure 36a shows a fabricated IR rectenna for 10μm radiation. The IR rectenna is a simple half wave dipole antenna, where the rectifying element is a metal insulator metal (MIM) tunnel diode. This device uses a symmetric Ni electrode structure with a thin insulating NiO layer at the overlap region and is intended as a pixel in an IR detector and not for IR energy direct conversion. The circuit model for the diode is shown in Figure 36b where the diode is modeled as a capacitor C and resistor R_d. The antenna/transmission line is modeled as a series resistance. This simple picture is useful in helping in identifying shortcomings in the device design. In order for the diode to work as a lumped circuit element, its RC time constant must be on the order of the characteristic period of the radiation. For 10μm light, this implies that an approximately 30THz diode RC time constant is necessary. To achieve the appropriate RC time constant for a MIM tunnel diode, we must reduce the capacitance by reducing the overlap area of the diode seen in Figure 36a. The resulting tunnel current in the small overlap regions is very small. Figure 36c shows typical MIM tunnel diode I-V characteristics. Furthermore by thinning the metal lines leading to the tunnel diode overlap region, we find that the series resistance increases which degrades the RC time constant gains made by shrinking the capacitor area. We are thus in a trade-off regime where the simple lumped element diode rectifier does not allow for RC time constant scaling.

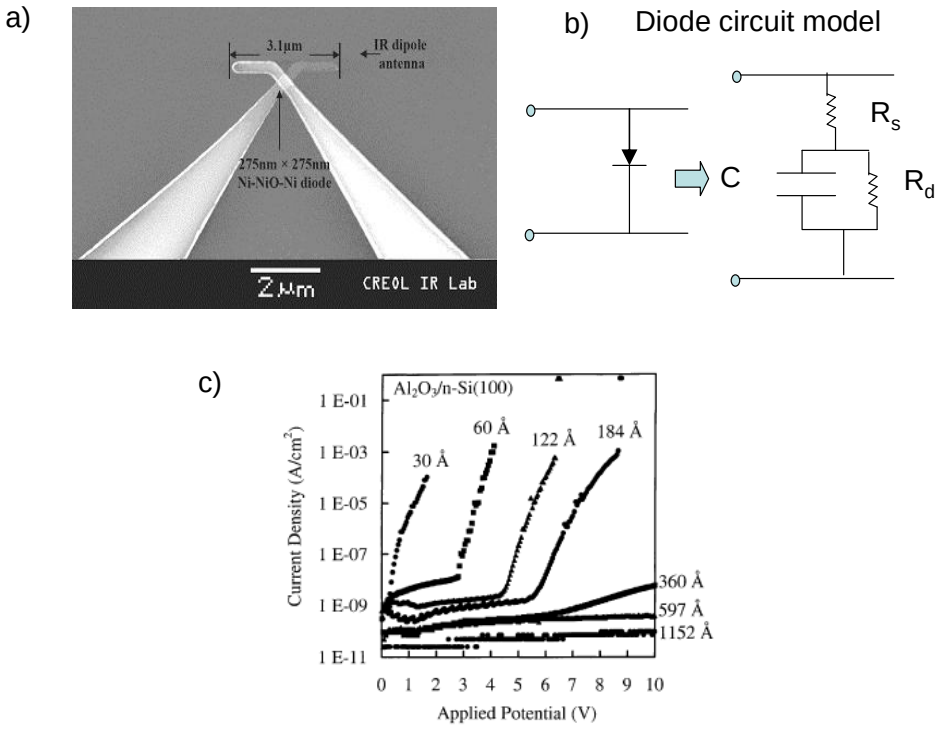

Figure 36. Example of IR rectenna design inspired by RF design. a) IR linear dipole rectenna with MIM tunnel diode rectifier b) Diode circuit model. R_d is diode differential resistance, C is diode capacitance and R_s is series resistance. c) Tunnel diode I-V characteristics.

6.1.1 Plasmonic Traveling Wave IR Rectenna

A new concept device based device based on a large area antenna and a distributed traveling wave MIM diode rectifier is proposed. The simple dipole antenna is replaced by a metallic 2D grating which is designed to efficiently convert the incident surface radiation into bound surface plasmon modes. These bound surface propagating modes are know to propagate into nanometer scale channels and it is this property we exploit to construct the traveling wave rectifier. Figure 37 illustrates directional coupling of to a surface plasmon and propagation in nanometer channels. In the example, the evanescent mode tail in dielectric waveguide is used to phase match into a guided surface mode. This mode is a collective excitation of the electron density in the metal and is tightly bond to the metallic surface. This enables the mode to propagate into nanometer scale channels which is required for our traveling wave rectification scheme.

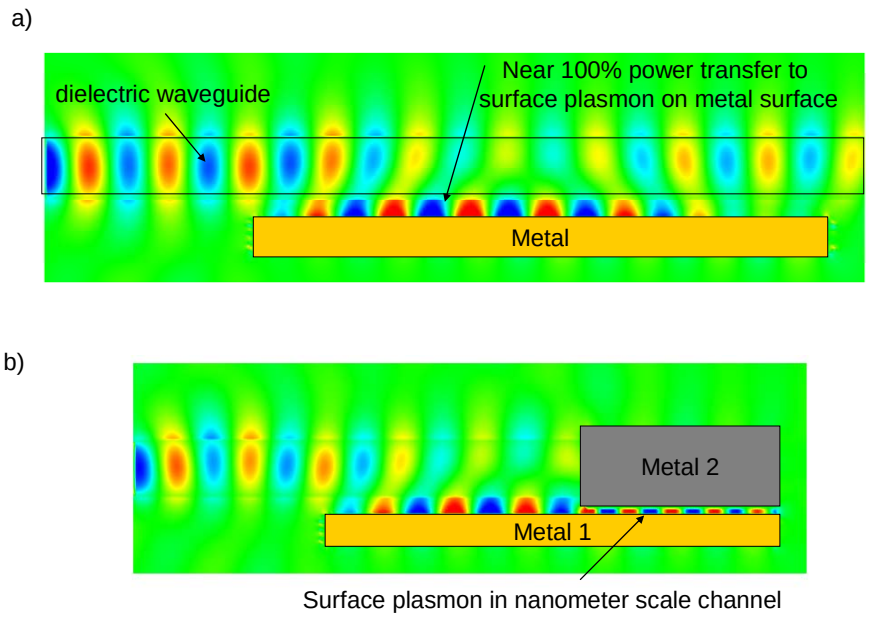

Figure 37. Illustrative example of a) surface plasmon directional coupling b) propagation into nanometer scale channels.

The plasmonic traveling wave rectifier consists of two key elements: a) a large area antenna for conversion of the incident radiation into a guided surface electromagnetic mode, b) a rectifying metal insulator metal (MIM) tunnel diode. In the following sections, we will review progress in the design and fabrication of these individual elements with an eye toward integration for the thermal energy harvesting application.

6.1.2 Plasmonic Antenna

We have developed multi-layered plasmonic antenna structures under the Plasmonic Anti-reflective coating (PARC) LDRD. These structures are designed to absorb the incident radiation in a narrow band of the Mid-IR spectrum. This strong absorption is independent of incident angle and polarization and represents near perfect impedance matching of the antenna to free-space. Figure 38 shows the design of an optimized IR absorber. We utilize the measured n and k dispersion of all the CMOS fab materials and design the ground plane and matched layer for optimal absorption depth and bandwidth. The front surface Au frequency selective surface (FSS) is designed for maximizing the transmission into the matched stack/ground plane configuration. The patterned FSS is formed using standard e-beam techniques and a comparison to the measured and theoretically predicted RCWA expression for the polarization averaged reflection is seen to be quite good. It should be noted that the average reflection at 8.4μm is 0.05% or less and is insensitive to the angle of incidence.

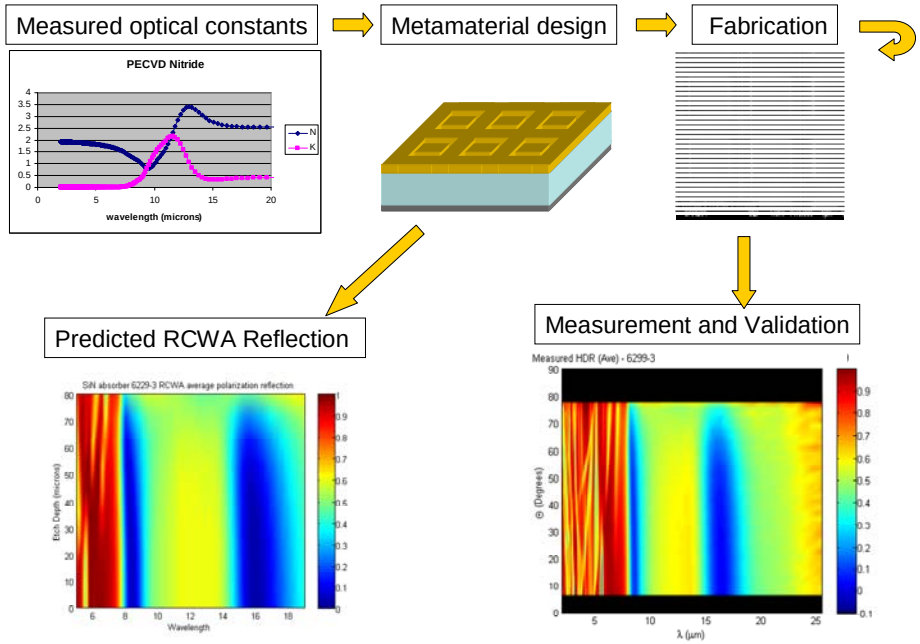

Figure 38. Design flow of a structured IR absorber fabricated and tested under PARC LDRD. The multilayered stack is optimized to give greater than 95% absorption in a band around 8.4 microns.

The realization of a thermal energy harvesting device requires the integration of the large area plasmonic antenna with the MIM tunnel diode for rectification. Currently, we are pursuing fabrication and integration of the MIM diode into plasmonic antenna structures for novel sensing and IR energy harvesting applications.

7. SUMMARY

Plasmonic structures open up new opportunities in photonic devices, sometimes offering an alternate method to perform a function and sometimes offering capabilities not possible with standard optics. In this LDRD we successfully demonstrated metal coatings on optical surfaces that do not adversely affect the transmission of those surfaces at the design frequency. This technology could be applied as an RF noise blocking layer across an optical aperture or as a method to apply an electric field to an active electro-optic device without affecting optical performance. We also demonstrated thin optical absorbers using similar patterned surfaces. These infrared optical antennas show promise as a method to improve performance in mercury cadmium telluride detectors. Furthermore, these structures could be coupled with other components to lead to direct rectification of infrared radiation. This possibility leads to a new method for infrared detection and energy harvesting of infrared radiation.

8. References

1. G. R. Hadley, *J. Comp. Phys*., **203**, 358-370(2005).

Distribution

4 Lawrence Livermore National Laboratory
Attn: N. Dunipace (1)
P.O. Box 808, MS L-795
Livermore, CA 94551-0808

1	MS0123	D. Chavez, LDRD Office	1011	
1	MS0529	Jacques Loui	5345	
1	MS0899	Technical Library	9536	(electronic copy)
1	MS1082	Alvaro Cruz-Cabrera	1725	
1	MS1082	Paul Davids	1727	
1	MS1082	Shanalyn Kemme	1725	
1	MS1082	Rick McCormick	1727	
1	MS1082	David Peters	1727	
1	MS1082	Joel Wendt	1725	
1	MS1152	Lorena Basilio	1653	
1	MS1152	William Johnson	1653	
1	MS1330	Jim Hudgens	5340	


Sandia National Laboratories